

Atmospheric oxidation capacity and ozone pollution mechanism in a coastal city of Southeast China: Analysis of a typical photochemical episode by Observation-Based Model

Taotao Liu^{1,2,3}, Youwei Hong^{1,2}, Mengren Li^{1,2}, Lingling Xu^{1,2}, Jinsheng Chen^{1,2*}, Yahui Bian^{1,2}, Chen Yang^{1,2,3}, Yangbin Dan^{1,2}, Yingnan Zhang⁴, Likun Xue^{4*}, Min Zhao⁴, Zhi Huang⁵, Hong Wang⁶

¹Center for Excellence in Regional Atmospheric Environment, Institute of Urban Environment, Chinese Academy of Sciences, Xiamen, China

²Key Lab of Urban Environment and Health, Institute of Urban Environment, Chinese Academy of Sciences, Xiamen, China

³University of Chinese Academy of Sciences, Beijing, China

⁴Environment Research Institute, Shandong University, Jinan, Shandong, China

⁵Xiamen Institute of Environmental Science, Xiamen, China

⁶Fujian Meteorological Science Institute, Fujian Key Laboratory of Severe Weather, Fuzhou, China

Corresponding authors E-mail: Jinsheng Chen (jschen@iue.ac.cn); Likun Xue (xuelikun@sdu.edu.cn)

Abstract:

A typical multi-day ozone (O₃) pollution event was chosen to explore the atmospheric oxidation capacity (AOC), OH reactivity, radical chemistry, and O₃ pollution mechanism in a coastal city of Southeast China, with an Observation-Based Model coupled to the Master Chemical Mechanism (OBM-MCM). The hydroxyl radical (OH) was the predominant oxidant (90±25%) for daytime AOC, while NO₃ radical played an important role for AOC during the nighttime (72±9%). Oxygenated volatile organic compounds (OVOCs, 30±8%), NO₂ (29±8%) and CO (25±5%) were the dominant contributors to OH reactivity, accelerating the production of O₃ and recycling of ROx radicals (ROx=OH+HO₂+RO₂). Photolysis of nitrous acid (HONO, 33±14%), O₃ (25±13%), formaldehyde (HCHO, 20±5%), and other OVOCs (17±2%) were major ROx sources, which played initiation roles in atmospheric oxidation processes. Combined with regional transport analysis, the reasons for this O₃ episode were the accumulation of local photochemical production and regional transport. The results of sensitivity analysis showed that VOCs were the limiting factor of radical recycling and O₃ formation, and the 5% reduction of O₃ would be achieved by decreasing 20% anthropogenic VOCs, and controlling emissions of aromatics, alkenes, and alkanes with ≥4 carbons were benefit for ozone pollution mitigation. The findings of this study have significant guidance for emission reduction and regional collaboration on future photochemical pollution control in the relatively clean coastal cities of China and similar countries.

Keywords: Atmospheric oxidation capacity; Radical chemistry; O₃ formation mechanism; OH reactivity;

39 **1 Introduction**

40 Tropospheric ozone (O_3) is mainly produced by photochemical reactions of anthropogenic and
41 natural emitted volatile organic compounds (VOCs) and nitrogen oxides (NO_x), and is an important factor
42 resulting in regional air pollution (Zhu et al., 2020; Lu et al., 2018). The elevated O_3 concentrations
43 enhance the atmospheric oxidation capacity (AOC) and have harmful effects on global climate change,
44 ecosystems, and human health (Liu et al., 2019a; Fowler et al., 2009). The formation mechanisms of O_3
45 pollution are extremely difficult to figure out, due to the complex types and sources of its precursors
46 (Simon et al., 2015). O_3 formation is affected by multiple factors such as O_3 precursor speciation or level,
47 atmospheric oxidation capacity, meteorological conditions and regional transport (Gong and Liao, 2019;
48 Chang et al., 2019). To effectively control the tropospheric O_3 pollution, exploration of the photochemical
49 mechanism and judgment on the controlling factors of O_3 formation become extremely important for
50 scientific community (Chen et al., 2020; Li et al., 2018).

51 The atmospheric oxidation capacity reflects the essential driving force in tropospheric chemistry,
52 and plays an important place in the loss rates of primary components and production rates of secondary
53 pollutants, thus the key factors to quantify AOC are processes and rates of species being oxidized in the
54 atmosphere (Elshorbany et al., 2009). The atmospheric conditions (such as photolysis rate, meteorology,
55 pollutant concentrations and regional transport) together influence the AOC levels, and the AOC levels
56 in the polluted urban regions are generally much higher than those at the background sites or remote
57 regions due to the dominant limited factor for the significant differences of pollutant concentrations (Geyer
58 et al., 2001; Xue et al., 2016). ROx radicals, including hydroxyl radical (OH), hydro peroxy radical (HO_2)
59 and organic peroxy radical (RO_2), are very important indicators in atmospheric photochemistry and
60 dominate the atmospheric oxidation capacity (Li et al., 2018). Meanwhile, radical chemistry drives the
61 transformation and recycling of O_3 through initiating atmospheric oxidation processes (Wang et al., 2020).
62 Among these radicals, the OH radical accounts for the majority of AOC over 90% during the daytime,
63 thus the OH reactivity (i.e., OH loss) indicates the primary contribution of individual pollutants (Wang et
64 al., 2018a; Mao et al., 2010). Hence, atmospheric oxidation capacity, OH reactivity, and radical chemistry
65 are crucial aspects for understanding the complex atmospheric photochemistry processes (Li et al., 2018).
66 For example, the major ROx sources are the photolysis reaction of O_3 , formaldehyde (HCHO), other
67 oxygenated volatile organic compounds (OVOCs), nitrous acid (HONO) and the reactions of O_3 with
68 unsaturated VOCs (Volkamer et al., 2010). The dominant ROx sources at some rural sites were O_3

69 photolysis and O₃ reactions with VOCs (Li et al., 2018; Martinez et al., 2003), and those at many urban
70 sites were HONO and OVOCs photolysis (Xue et al., 2016; Liu et al., 2012; Emmerson et al., 2005). For
71 oil and gas field sites, there were highly abundant VOCs to promote the formations of O₃, and the
72 contribution of OVOCs photolysis was 2-5 times higher than that in urban areas (Chen et al., 2020;
73 Edwards et al., 2013, 2014). The HONO photolysis was a very important ROx source at the high-altitude
74 or background sites. (Acker et al., 2001; Jiang et al., 2020).

75 Current studies of atmospheric O₃ photochemical pollution observations have been conducted at the
76 urban, suburban, rural and remote sites around the world (Smith et al., 2006; Eisele et al., 1997; Kanaya
77 et al., 2001; Hofzumahaus et al., 2009; George et al., 1999; Emmerson et al., 2005; Kanaya et al., 2007;
78 Michoud et al., 2012). In China, O₃ photochemical pollution events have been reported in some megacities,
79 such as Beijing, Shanghai, Guangzhou, and Chengdu (Liu et al., 2012; Tan et al., 2019; Zhu et al., 2020;
80 Wang et al., 2020; Liu et al., 2019b; Ling et al., 2017). Few studies on O₃ photochemical pollution in
81 cities with low O₃ precursor emissions have been reported, and the air quality in these areas usually
82 depends on the change of meteorological conditions. In a coastal city of Southeast China, the
83 concentrations of O₃ precursors were higher than those in remote sites and background, but lower than
84 those in most urban and suburban areas, even lower than those in rural regions (Table S1). In a word, O₃
85 precursor emissions in our observation site were relatively low. Meanwhile, the southeast coastal region
86 is influenced by the East Asian monsoon and acts as an important transport path between the Yangtze
87 River Delta (YRD) and the Pearl River Delta (PRD) (Liu et al., 2020a; Liu et al., 2020b), which is a good
88 ‘laboratory’ to further explore O₃ photochemical pollution and formation mechanism with relatively low
89 O₃ precursors and complex meteorological conditions (Zhang et al., 2020b; Hu et al., 2020).

90 The Observation-Based Model (OBM) is widely used to investigate O₃-VOCs-NO_x relationships
91 and radical chemistry (Wang et al., 2018a; Tan et al., 2019). The O₃ sensitivity revealed the non-linear
92 relationship between O₃ and its precursors (i.e., VOCs and NO_x), which was conducted to investigate O₃
93 formation mechanism and control strategies (Wang et al., 2020). The OBM combined with the Master
94 Chemical Mechanism (V3.3.1) (OBM-MCM) has been applied to explore the O₃ photochemical pollution
95 mechanism in different environmental conditions (Chen et al., 2020; Li et al., 2018; Xue et al., 2016;
96 Wang et al., 2018). In this study, we chose a typical multi-day O₃ pollution event in the coastal city Xiamen
97 (Fig. S1), when Xiamen was affected by various meteorological conditions, such as typhoon and the West
98 Pacific Subtropical High (WPSH) accompanied by temperature inversion phenomenon. Based on the
99 OBM-MCM analyses, the study aims to clarify (1) the pollution characteristics of O₃ and its precursors,
100 (2) the atmospheric oxidation capacity and radical chemistry, and (3) the O₃ formation mechanism and
101 sensitivity analysis. The results are expected to enhance the understanding of the O₃ formation mechanism

with low O₃ precursor levels, and provide scientific evidence for O₃ pollution control in the coastal cities.

2 Materials and methods

2.1 Study area and field observations

Xiamen is a coastal city in the southeast area of China, to the west coast of the Taiwan Strait. The field campaigns were carried out at the Atmospheric Environment Observation Supersite (24.61° N, 118.06° E) on the rooftop of around 70 m high building in the Institute of Urban Environment, Chinese Academy of Sciences. The supersite was equipped with complete monitoring instruments, including gas and aerosol species compositions, O₃ precursors, meteorological parameters, and photolysis rate. Criteria air pollutants of O₃, SO₂, NO-NO₂-NO_x, and CO were monitored by commercial instruments TEI 49i, 43i, 42i, and 48i (*Thermo Fisher Scientific, USA*), respectively. The meteorological parameters of wind speed (WS), wind direction (WD), air temperature (T), pressure (P), and relative humidity (RH) were measured by an ultrasonic anemometer (*150WX, Airmar, USA*). HONO was measured with an analyzer for Monitoring Aerosols and Gases in Ambient Air (*MARGA, ADI 2080, Applikon Analytical B.V., the Netherlands*). A gas chromatography-mass spectrometer (GC-FID/MS, *TH-300B, Wuhan, CN*) was used for atmospheric VOCs concentrations monitoring, involving about 103 species of VOCs with a 1-hour time resolution. Photolysis frequencies were measured by a photolysis spectrometer (*PFS-100, Focused Photonics Inc., Hangzhou, China*). The photolysis rate constants include $J(\text{O}^1\text{D})$, $J(\text{NO}_2)$, $J(\text{H}_2\text{O}_2)$, $J(\text{HONO})$, $J(\text{HCHO})$, and $J(\text{NO}_3)$. Strict quality assurance and quality control were applied, and the detailed descriptions of the monitoring procedures were documented in our previous studies (Zhang et al., 2020b; Wu et al., 2020; Liu et al., 2020a; Liu et al., 2020b; Hu et al., 2020).

2.2 Observation-based chemical box model

In this study, the Observation-Based Model (OBM) combined with the latest version 3.3.1 of MCM (MCM v3.3.1; <http://mcm.leeds.ac.uk/MCM/>), involving 142 non-methane VOCs and more than 17000 elementary reactions of 6700 primary, secondary and radical species (Jenkin et al., 2003; Saunders et al., 2003), was used to explore the atmospheric oxidation processes and O₃ formation mechanisms. The physical process of deposition within the boundary layer height (BLH), which varied from 300 m during nighttime to 1500 m during the daytime in autumn (Li et al., 2018), was considered in the model. Therefore, the dry deposition velocity was utilized to simulate the deposition loss of some reactants in the atmosphere and showed in Table S2, which avoided continuous accumulation of pollutant concentrations in the model (Zhang et al., 2003; Xue et al., 2016).

The observation parameters of the gaseous pollutants (i.e., O₃, CO, NO, NO₂, HONO, SO₂, and VOCs), meteorological parameters (i.e., T, P, and RH), and photolysis rate constants ($J(O^1D)$, $J(NO_2)$, $J(H_2O_2)$, $J(HONO)$, $J(HCHO)$, and $J(NO_3)$) were input into the OBM-MCM model as constraints. The photolysis rates of other molecules such as OVOCs were parameterized by solar zenith angle and then scaled by the measured $J(NO_2)$ (Saunders et al., 2003). We pre-ran for 5 days before running the model to initialize the unmeasured compounds and radicals (Xue et al., 2014).

OBM-MCM is mainly used to simulate in situ atmospheric photochemical processes and quantify the O₃ production rate, AOC, OH reactivity, and ROx radical budgets. Among them, primary sources of ROx, including the photolysis reactions of O₃, HONO, formaldehyde (HCHO), and other OVOCs as well as reactions of VOCs with O₃ and NO₃ radicals, are important (Xue et al., 2016). The termination reactions of ROx are controlled by cross-reactions with NOx (under high NOx conditions) and ROx (under low NOx conditions) to form nitric acid, organic nitrates, and peroxides (Liu et al., 2012; Xue et al., 2016). Table 1 shows the production and destruction reactions and relevant reaction rates of O₃ in our study. The production rate of O₃ (P(O₃)) includes RO₂+NO (R1) and HO₂+NO reactions (R2, Eq. 1), and the destruction of O₃ (D(O₃)) involves reactions of O₃ photolysis (R3), O₃+OH (R4), O₃+HO₂ (R5), NO₂+OH (R6), O₃+VOCs (R7), and NO₃+VOCs (R8, Eq. 2). The net O₃ production rate (Pnet(O₃)) is calculated by P(O₃) minus D(O₃) as equation 3.

Table 1. Simulated production and destruction reactions and relevant reaction rates of O₃ in our study.

Reactions	Reaction rates	Number
O₃ production pathways-P(O₃)		
RO ₂ +NO→RO+NO ₂	$2.7 \times 10^{-12} \times \text{EXP}(360/T)$	R1
HO ₂ +NO→OH+NO ₂	$3.45 \times 10^{-12} \times \text{EXP}(270/T)$	R2
O₃ loss pathways-D(O₃)		
O ₃ +hν→O ¹ D+O ₂	JO ¹ D	R3a
O ¹ D+H ₂ O→OH	2.14×10^{-10}	R3b
O ₃ +OH→HO ₂	$1.70 \times 10^{-12} \times \text{EXP}(-940/T)$	R4
O ₃ +HO ₂ →OH	$2.03 \times 10^{-16} \times (T/300)^{4.57} \times \text{EXP}(693/T)$	R5
NO ₂ +OH→HNO ₃	$3.2 \times 10^{-30} \times 9.7 \times 10^{18} \times P/T \times (T/300)^{-4.5} \times 3.0^{11} \times 10^{\log_{10}(0.41)} / (1 + (\log(3.2^{-30} \times 9.7 \times 10^{18} \times P/T \times (T/300)^{-4.5} \times 3.0^{11} \times 10^{\log_{10}(0.41)} / (0.75 - 1.27 \times (\log_{10}(0.14))^2) / (3.2^{-30} \times 9.7 \times 10^{18} \times P/T \times (T/300)^{-4.5} + 3.0^{-11}))^2) / (3.2^{-30} \times 9.7 \times 10^{18} \times P/T \times (T/300)^{-4.5} + 3.0^{-11}))$	R6
O ₃ +VOCs→Carbonyls+Criegee biradical	Kcons.1	R7
NO ₃ +VOCs→RO ₂	Kcons.2	R8

Note: The reaction rates of Kcons.1 and Kcons.2 were constant. There were around 700 reactions of VOCs+NO₃/O₃, and the relevant reaction rates were different, which can be obtained from this website <http://mcm.leeds.ac.uk/MCM/>.

$$P(O_3) = k_1[HO_2][NO] + \sum(k_{2i}[RO_2][NO]) \quad (1)$$

$$D(O_3) = k_3[O_1D][H_2O] + k_4[O_3][OH] + k_5[O_3][HO_2] + k_6[NO_2][OH] + \sum(k_{7i}[O_3][unsat.VOCs]) + 2\sum(k_{8i}[NO_3][unsat.VOCs]) \quad (2)$$

$$P_{net}(O_3) = P(O_3) - D(O_3) \quad (3)$$

where k_i is the related reaction rate constant. Detailed descriptions of the chemistry calculation can be found elsewhere (Chen et al., 2020; Wang et al., 2018a; Xue et al., 2014).

Relative incremental reactivity (RIR), an index to diagnose the sensitivity of O_3 formation to precursors, is defined as the ratio of the differences in O_3 production rate to the difference in precursor concentrations (Chen et al., 2020). Here, the $\Delta X/X$ in the OBM-MCM represents the percentage reduction in the input concentrations of each targeted O_3 precursor group and this value is adopted as 20% (Liu et al., 2020c).

$$RIR = \frac{\Delta P(O_3)/P(O_3)}{\Delta X/X} \quad (4)$$

2.3 Model performance

The index of agreement (IOA) can be used to judge the reliability of the model simulation results, and its equation is (Liu et al., 2019b):

$$IOA = 1 - \frac{\sum_{i=1}^n (O_i - S_i)^2}{\sum_{i=1}^n (|O_i - \bar{O}| + |S_i - \bar{O}|)^2} \quad (5)$$

where S_i is simulated value, O_i represent observed value, \bar{O} the average observed values, and n is the sample number. The IOA range is 0-1, and the higher the IOA value is, the better agreement between simulated and observed values is. In many studies, when IOA ranges from 0.68 to 0.89 (Wang et al., 2018b), the simulation results are reasonable, and the IOA in our research is 0.80. Hence, the performance of the OBM-MCM model was reasonably acceptable.

2.4 Meteorological data and back trajectory calculation

The backward trajectories of air masses arriving at the observation site were calculated by the MeteoInfo during the episode (Wang *et al.*, 2014). The backward trajectories with 72-h were run with the time resolution of 3 hours at 100 m height above ground level, and starting time was 0:00 LT and the ending time was 23:00 LT. Meteorological data were provided by NOAA ARL (<ftp://arlftp.arlhq.noaa.gov/pub/archives/gdas1>). The Final Operational Global Analysis data (FNL) is from the Global Data Assimilation System and analyzes results with the model which is also used by the National Center for Environmental Prediction (NCEP) in the Global Forecast System (GFS)

186 (<https://rda.ucar.edu/datasets/ds083.2/>). The weather charts were conducted using Grid Analysis and
187 Display System (GrADS) with the specific programmed script files. A detailed description of the synoptic
188 information was shown in our previous study (Wu et al., 2019).

189 **3 Results and discussion**

190 **3.1 Overview of observations**

191 The O₃ pollution events frequently appeared in the coastal city Xiamen during autumn time, related
192 to the WPSH, carrying favorable photochemical reaction conditions (high temperature, low RH, and
193 stagnant weather conditions) and encouraging the formation and accumulation of O₃ in the southeast
194 coastal area (Wang et al., 2018a). The daily maximum 8-h-average O₃ concentrations (MDA8h O₃) from
195 20 to 29 Sep 2019 ranged from 53 to 85 ppbv, partly exceeding the Grade II of China's National Ambient
196 Air Quality Standard of 75 ppbv. The time series and descriptive statistics of air pollutants and
197 meteorological parameters during this multi-day O₃ pollution event are shown in Fig. 1 and Table 2.
198 During this period, the dominant wind direction was northeast, with an average wind speed of 1.8 ± 0.9
199 $\text{m} \cdot \text{s}^{-1}$. The maximum hourly temperature was as high as 35 °C, and the average RH was $56.4 \pm 12.6\%$. Our
200 previous study showed that particulate pollution was slight in Xiamen, which could affect solar radiation
201 by light-absorbing component, and the concentrations of particulate matter had not exceeded the National
202 Ambient Air Quality Standard (Class II: $75 \mu\text{g} \cdot \text{m}^{-3}$) for a whole year (Hu et al., 2021; Deng et al., 2020).
203 Therefore, solar radiation intensity and J(NO₂) were strong, compared to those of the Yellow River Delta
204 (Chen et al., 2020), Shanghai (Zhu et al., 2020) and Hong Kong (Xue et al., 2016). In general, these
205 meteorological parameters were conducive to the production and accumulation of O₃. In addition, O₃
206 concentrations at nighttime kept relatively high (Fig.1), indicating the influence of regional transport and
207 little NO titration (Zhang et al., 2020a; Wu et al., 2020). Figure S2 shows the 72 h back trajectories at the
208 monitoring site. Among them, 80% of the air masses came from the Yellow Sea, and the other 20% air
209 masses originated from the northeast China through long-range transport.

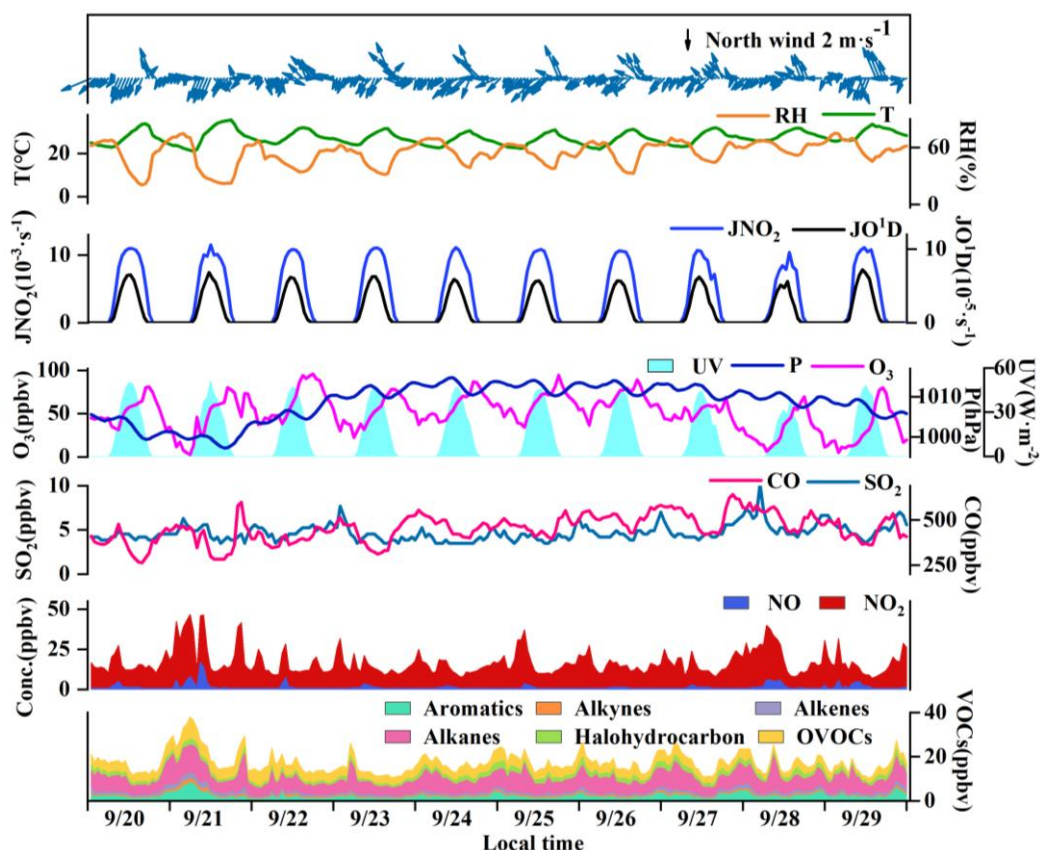


Figure 1. Time series of major trace gases, photolysis rate constants, and meteorological parameters during 20-29 Sep. 2019 in Xiamen.

Table 2. Descriptive statistics of major trace gases (ppbv) and meteorological parameters during 20-29 Sep. 2019.

Parameters	Mean±SD	Median	Max
MDA8h O ₃	67.4±17.2	52.6	89.3
TVOCs	17.2±4.8	16.1	38.0
CO	452±77.3	454	641
NO	1.4±1.3	0.8	17.1
NO ₂	15.4±6.9	13.6	40.9
SO ₂	4.7±0.9	4.6	10.2
T (°C)	27.3±3.21	26.9	35.6
RH (%)	56.4±12.6	56.6	75.0
P (hPa)	1008±4.57	1010	1015
UV (W·m ⁻²)	46.4±1.12	0	51.1
Wind speed (m·s ⁻¹)	1.8±0.9	1.6	3.8
Wind direction (°)	90.8±90.4	45.0	337

Table 3. Measured VOCs concentrations during 20-29 Sep. 2019 in Xiamen (Units: pptv), and the classification of VOCs were used and introduced in Section 3.3.

Chemicals	Classification	Mean±SD	Chemicals	Classification	Mean±SD
Aromatics		2131±1236	Alkanes		6970±2325
toluene	RAROM/AHC	995±632	ethane	LRHC/AHC	1552±342
m/p-xylene	RAROM/AHC	392±326	propane	LRHC/AHC	1546±608
benzene	LRHC/AHC	236±95	iso-pentane	C4HC/AHC	930±316
o-xylene	RAROM/AHC	154±121	n-butane	C4HC/AHC	844±365
ethylbenzene	RAROM/AHC	138±94	n-dodecane	C4HC/AHC	618±101
styrene	RAROM/AHC	76±65	iso-butane	C4HC/AHC	494±201
1,2,4-trimethylbenzene	RAROM/AHC	75±37	n-pentane	C4HC/AHC	254±157

m-ethyltoluene	RAROM/AHC	16±11	n-hexane	C4HC/AHC	134±184
p-ethyltoluene	RAROM/AHC	10±6	3-methylhexane	C4HC/AHC	116±93
iso-propylbenzene	RAROM/AHC	5±3	n-heptane	C4HC/AHC	104±78
1,3,5-trimethylbenzene	RAROM/AHC	8±6	3-methylpentane	C4HC/AHC	82±48
o-ethyltoluene	RAROM/AHC	8±5	2-methylhexane	C4HC/AHC	67±38
1,2,3-trimethylbenzene	RAROM/AHC	7±5	2-methylpentane	C4HC/AHC	56±46
n-propylbenzene	RAROM/AHC	7±4	2,3-dimethylbutane	C4HC/AHC	54±33
Halocarbons		1951±572	cyclohexane	C4HC/AHC	42±15
dichloromethane	AHC	998±392	n-undecane	C4HC/AHC	33±35
1,2-dichloroethane	AHC	499±210	n-octane	C4HC/AHC	24±15
chloromethane	AHC	294±75	n-nonane	C4HC/AHC	15±13
1,2-dichloropropane	AHC	88±34	2,2-dimethylbutane	C4HC/AHC	15±7
bromomethane	AHC	47±23	n-decane	C4HC/AHC	14±11
trichloroethene	AHC	15±6	Alkenes		1205±464
1,4-dichlorobenzene	AHC	9±3	ethene	Alkenes/AHC	671±361
OVOCs	AHC	4246±1263	propene	Alkenes/AHC	207±116
acetone	AHC	2802±750	isoprene	BHC	171±232
2-butanone	AHC	799±430	trans-2-pentene	Alkenes/AHC	105±62
2-propanol	AHC	343±283	1-butene	Alkenes/AHC	16±21
2-methoxy-2-methylpropane	AHC	169±97	cis-2-butene	Alkenes/AHC	12±12
acrolein	AHC	66±22	1-pentene	Alkenes/AHC	10±7
4-methyl-2-pentanone	AHC	16±15	1,3-butadiene	Alkenes/AHC	8±7
2-hexanone	AHC	12±3	trans-2-butene	Alkenes/AHC	4±4
			Acetylene	LRHC/AHC	674±290

Table 3 lists the detailed VOCs concentrations during the observation period. Alkanes (6970±2325 pptv) were the predominant components of total VOCs, followed by OVOCs (4246±1263 pptv), aromatics (2131±1236 pptv), halocarbons (1951±572 pptv), alkenes (1205±464 pptv), and acetylene (674±290 pptv). The ratio of ethene/ethane (0.4±0.2) was significantly ($p<0.05$) lower than that in Hong Kong (0.7±0.1) with significant aged air masses, indicating that the high O₃ in Xiamen might be partially attributed to the aged air masses (e.g., transport of air from polluted regions or intense atmospheric oxidation) (Wang et al., 2018a). The concentration of TVOCs in Xiamen (17.2±4.8 ppbv) was much lower than that in the developed areas with large anthropogenic emissions (i.e., Beijing (44.2 ppbv), Lanzhou (45.3 ppbv), Wuhan (30.2 ppbv), Chengdu (36.0 ppbv), Hong Kong (26.9 ppbv), Los Angeles (41.3 ppbv) and Tokyo (43.4 ppbv), but was higher than that at the background and remote sites (i.e., Mt. Wuyi 4.7 ppbv and Mt. Waliguan 2.6 ppbv) (Table S1).

The O₃ formation process depends on its precursors and related environmental conditions, while the photochemical reactions during the daytime are the basis for O₃ changes. Figure 2 shows the diurnal patterns of major trace gases and meteorological parameters during 20-29 Sep. 2019. The O₃ concentration was maintained at relatively low levels from night to 07:00 LT, then rose and reached its maximum at around 17:00 LT. O₃ peak in the afternoon was related to the accumulation of both local

photochemical reaction and potential regional transport (including O₃ and its precursors in the upwind direction to the observation site), and the detailed analysis will be shown in Section 3.3.2. The reduction of observed O₃ (Δ O₃) in the early morning rush hour caused by NO titration did not appear, verifying the impacts of regional transport (Liu et al., 2019b; Zeren et al., 2019; Chen et al., 2020). Due to the photochemical reactions, the precursors of CO, NO_x and VOCs were consumed during the daytime, and were accumulated during the nighttime with weak solar radiation. The diurnal patterns of VOCs, NO_x and CO were similar, with the highest concentrations at around 08:00 LT and then decreasing during 9:00~16:00 LT and increasing at night, which is related to the human activity emissions (especially vehicle exhaust) and the variations of boundary layer (Elshorbany et al., 2009; Hu et al., 2020).

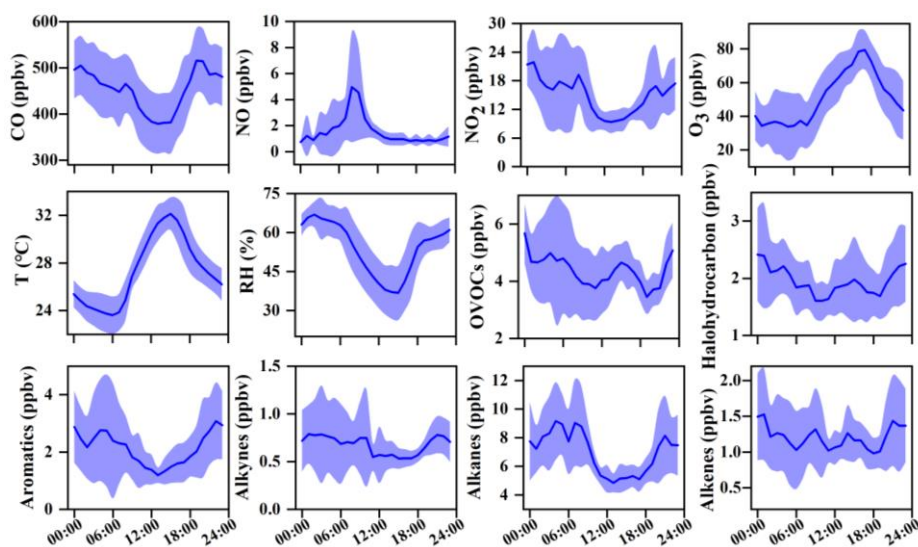


Figure 2. Average diurnal patterns of major trace gases and meteorological parameters during 20-29 Sep. 2019 in Xiamen. The error bar is the standard error.

3.2 Atmospheric oxidation and radical chemistry

3.2.1 Atmospheric oxidation capacity (AOC)

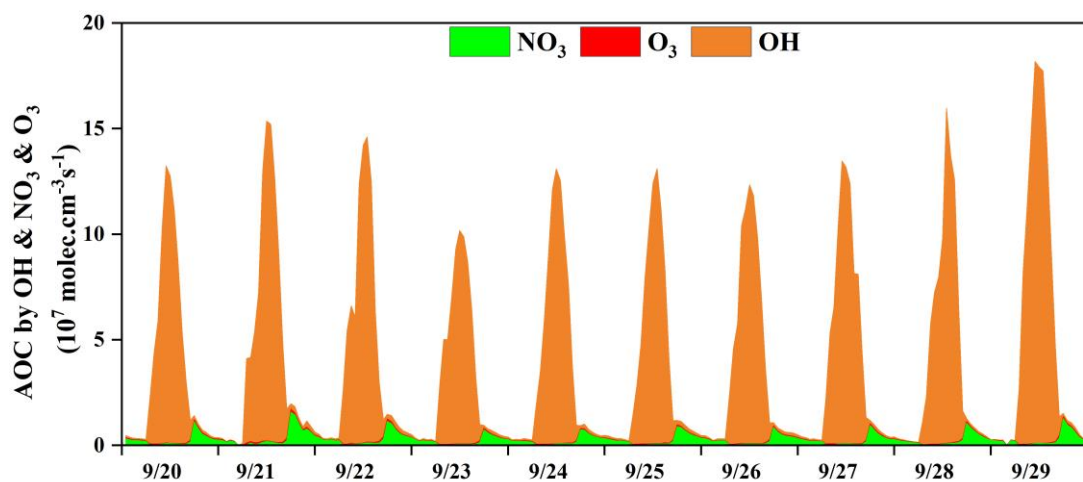


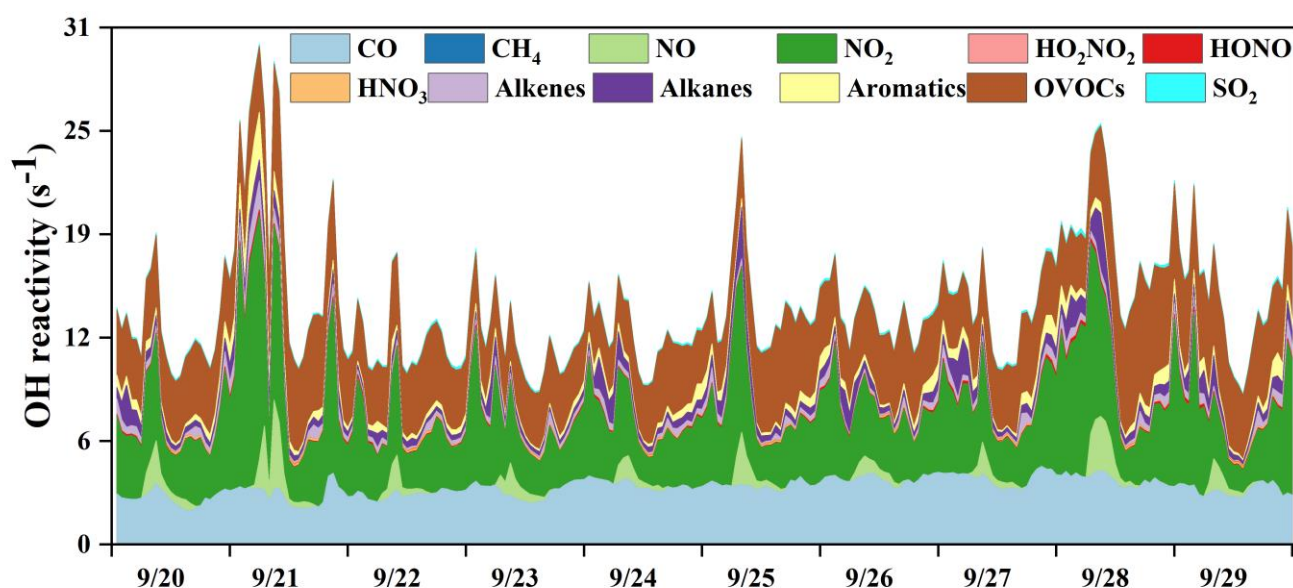
Figure 3. Time series of the model-calculated Atmospheric Oxidation Capacity (AOC) in Xiamen during 20-29 Sep. 2019.

Figure 3 shows the time series of the model-calculated AOC during the O₃ pollution period. The AOC determines the removal rate of primary pollutants and the production rate of secondary pollutants, and was the basis for reflecting atmospheric photochemical pollution (Geyer et al., 2001). AOC is calculated as the sum of oxidation rates of various primary pollutants (CO, NO_x, VOCs, etc.) by the major oxidants (i.e., OH, O₃, NO₃) (Chen et al., 2020; Xue et al., 2016; Xue et al., 2014). In this study, the average daytime AOC was 6.7×10^7 molecules $\text{cm}^{-3} \text{s}^{-1}$, and the daily maximum AOC was 1.3×10^8 molecules $\text{cm}^{-3} \text{s}^{-1}$, which was higher than those at rural sites with much low pollution emissions in Berlin (1.4×10^7 molecules $\text{cm}^{-3} \text{s}^{-1}$) and a regional background in Hong Kong (6.2×10^7), but lower than that in polluted cities, such as Santiago (3.2×10^8 molecules $\text{cm}^{-3} \text{s}^{-1}$), due to the main limited factor of the significant differences of pollutant concentrations among different sites (Li et al., 2018; Xue et al., 2016; Geyer et al., 2001; Zhu et al., 2020). In some urban regions, the concentrations of air pollutants were higher than those in Xiamen, but their AOC levels (Hong Kong: 1.3×10^8 molecules $\text{cm}^{-3} \text{s}^{-1}$; Shanghai: 1.0×10^8 molecules $\text{cm}^{-3} \text{s}^{-1}$) were comparable to or even lower compared with the AOC in Xiamen, which could be attributed to the relatively high solar radiation (Xue et al., 2016; Zhu et al., 2020) (Detailed descriptions showed in Section 3.1). The results of AOC characteristics in different regions were decided by the precursor concentrations/types and photochemical environment.

According to the diurnal patterns of the AOC contributed by OH, O₃, and NO₃, the predominant oxidant was OH ($90 \pm 25\%$) during the daytime, followed by NO₃ ($8 \pm 22\%$) and O₃ ($2 \pm 3\%$). Meanwhile, the diurnal characteristics of AOC were consistent with the profile of the model-calculated OH (Fig. S3) and the observed photolysis rate constants (Fig.1) (Zhu et al., 2020). Meanwhile, NO₃ ($72 \pm 9\%$) played the most important role in the oxidant capability during the nighttime, followed by OH ($20 \pm 12\%$) and O₃

276 (8±1%). In particular, the contribution of NO₃ to AOC reached the maximum of 80% at around 18:00 LT,
 277 when the concentrations of O₃ and NO₂ were relatively high and accelerated the formation of NO₃ (Fig.2).
 278 In addition, solar radiation was weak during the nighttime, which resulted in the accumulation of NO₃
 279 due to the cease of photolysis of NO₃ (Rollins et al., 2012; Chen et al., 2020). AOC contributed by O₃
 280 was negligible, owing to the relatively low concentration of alkenes at the monitoring site (Fig.1 and
 281 Table 3), since O₃ contributed to the oxidation capacity through alkenes ozonolysis (Xue et al., 2016). In
 282 summary, the OH radical dominated the AOC, and it was necessary to further explore the partitioning of
 283 OH reactivity among different precursor groups.

284

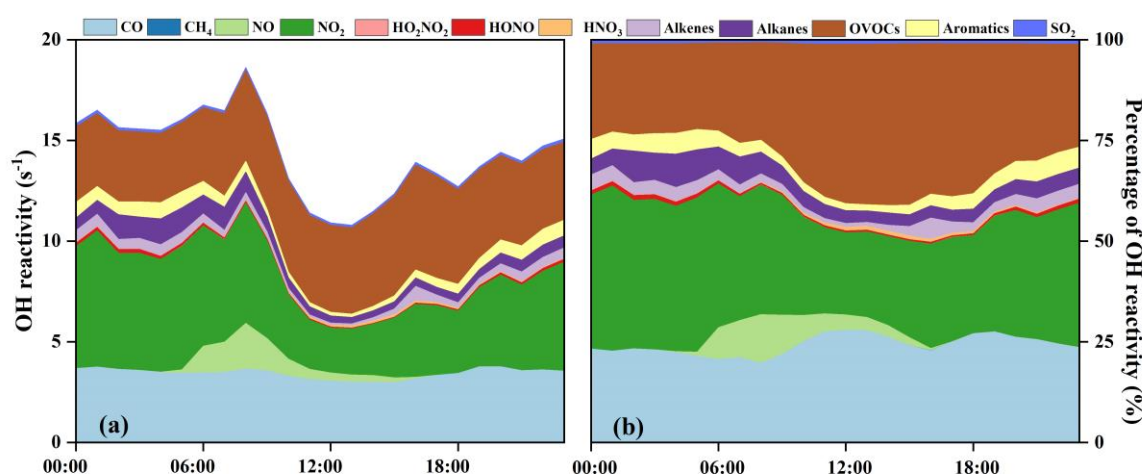


285

286 **Figure 4. Time series of model-calculated OH reactivity and its partitioning to the major reactants in Xiamen**
 287 **during 20-29 Sep. 2019.**

288

289



290

291 **Figure 5. (a) Diurnal patterns and (b) percentage of model-calculated OH reactivity and its partitioning to the**

292 **major reactants.**

293 The OH reactivity is an indicator for the OH chemical loss frequency, computed as the reaction rates
294 of OH with CO, NO_x, SO₂, HONO, HNO₃, HO₂NO₂, and VOCs (Whalley et al., 2016; Chen et al., 2020).
295 Time series and diurnal patterns of model-calculated OH reactivity as well as its partitioning to the major
296 reactants during the episode are shown in Fig. 4 and Fig. 5. The OH reactivity reached the peak (18.6 ± 4.8
297 s^{-1}) at around 8:00 LT, mainly caused by the reaction of OH with NO_x, since vehicles exhausted large
298 amounts of NO_x during rush hours. The average daily OH reactivity was $14.4 \pm 3.83 \text{ s}^{-1}$, which was much
299 lower than those in some polluted regions in Santiago (42 s^{-1}) and the PRD (50 s^{-1}), comparable to that
300 at a rural site in Nashville (11 s^{-1}), but higher than that at a mountain site in Pennsylvania (6 s^{-1})
301 (Elshorbany et al., 2009; Lou et al., 2010a; Lou et al., 2010b; Kovacs et al., 2003; Ren et al., 2005). Figure
302 5 shows the diurnal variations and percentage of model-calculated OH reactivity to the major reactants
303 during the episode. The OH reactivity exhibited a morning peak caused by the reactions of NO with OH,
304 which should be ascribed to the freshly emitted urban plumes. Anymore, OVOCs showed high fractions
305 at around 12:00-18:00 LT, which were mainly owing to the transport of the regional air masses containing
306 the abundant OVOCs, as well as the oxidation effect by strong photochemical process. As shown in
307 Fig. 5b, OVOCs ($30 \pm 8 \%$), NO₂ ($29 \pm 8\%$) and CO ($25 \pm 5\%$), were the dominant contributors to OH
308 reactivity, followed by alkanes ($5 \pm 3\%$), aromatics ($3 \pm 2\%$), alkenes ($3 \pm 1\%$), and NO ($2 \pm 4\%$). The high
309 fraction of OVOCs and NO₂ in OH reactivity indicated the high aged degree of air mass and the intensive
310 NO_x emissions during the observation period, respectively (Li et al., 2018). However, the fraction of CO
311 to OH reactivity at our observation site was higher than that at an urban site in Los Angeles (Hansen et
312 al., 2021), a rural site in Hong Kong (Li et al., 2018), and a mountain site in Colorado (Nakashima et al.,
313 2014), comparable to that at the urban site of Shanghai (Zhang et al., 2021a), which could be attributed
314 to the abundant CO in our observation site. CO mainly comes from vehicle exhaust and the combustion
315 of fossil fuels, and the observation site is a city with high density vehicles. Meanwhile, this pollution
316 event was under the influence of the WPSH, which promoted the formation and accumulation of
317 pollutants. The partitioning of OH reactivity elucidated the inherent photochemical processes and major
318 reactants in Southeast China. High OH reactivity of OVOCs, NO₂, and CO would promote the production
319 of RO_x radical. Therefore, the investigation of detailed chemical budget of the RO_x, recycling, and
320 termination reaction is meaningful to figure out the complex atmospheric photochemistry (Li et al., 2018;
321 Lou et al., 2010b).

322 **3.2.2 Radical chemistry**

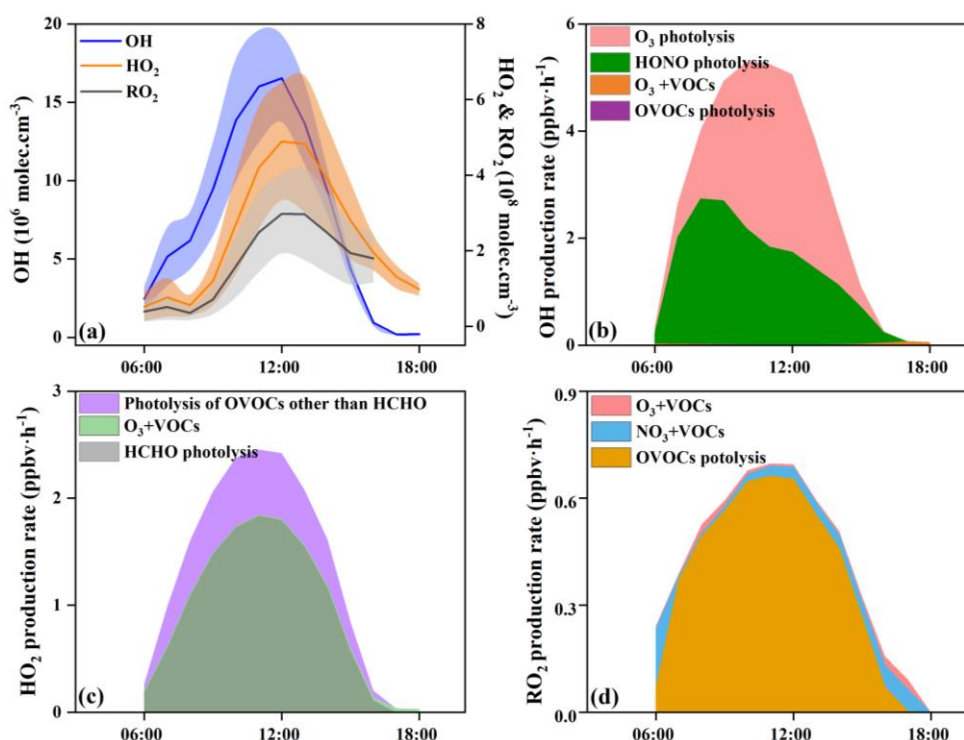


Figure 6. Model-simulated daytime average diurnal variations in (a) OH, HO₂, and RO₂ concentrations, and average primary production rates of (b) OH, (c) HO₂, and (d) RO₂ during 20-29 Sep. 2019 in Xiamen.

With the influence of NO_x and VOCs, RO_x radicals (OH, HO₂, and RO₂) undergo efficient recycling and produce secondary pollutants, such as O₃ and OVOCs (Sheehy et al., 2010). Figure 6 shows the model-simulated OH, HO₂, and RO₂ concentrations and their primary sources. The detailed time series of RO_x concentrations and chemical budget are summarized in Fig. S3. Figure 6a shows the diurnal variations of the simulated OH, HO₂, and RO₂. The maximum daily values of OH, HO₂, and RO₂ concentrations were 2.4×10^7 , 7.9×10^8 and 4.7×10^8 molecules.cm⁻³, with the daytime average concentrations of 7.4×10^6 , 2.4×10^8 and 1.7×10^8 molecules.cm⁻³, respectively. Model-predicted concentrations of OH in Xiamen were higher than that in the Yellow River Delta (an oil field with high VOCs emission), while the concentrations of HO₂ and RO₂ showed reverse trends (Chen et al., 2020). The RO_x recycling of OH→RO₂ was mainly controlled by the reaction of OH+VOCs, and the RO₂→HO₂ and HO₂→OH depended on the reactions with NO (Fig.7). Combined with the ratio of VOCs/NO_x (1.1 ± 0.4), it was convinced that NO_x would not be the limiting factor in the radical recycling processes. Hence, efficient conversions of radical propagation of RO₂+NO→HO₂ and HO₂+NO→OH were expected, and OH+VOCs→RO₂ reaction was the rate-depended step of the radical recycling in our study. The detailed radical chemistry would be further discussed as follows.

Figure 6b shows the daytime average diurnal variations of primary OH sources. HONO photolysis

reached the maximum of 2.7 ppb h^{-1} at around 8:00 LT, which occupied $56 \pm 19\%$ of the total OH primary production rates. The second source of OH primary production was O_3 photolysis ($42 \pm 21\%$), and the percentages of $\text{O}_3 + \text{VOCs}$ and OVOCs photolysis were minor. The highest HONO photolysis rate appeared in the morning rush hour, suggesting the influence of vehicle emissions and nocturnal accumulation of HONO (Hu et al., 2020). Considering the radical recycling, the reaction of $\text{HO}_2 + \text{NO}$ ($8.0 \pm 6.2 \text{ ppb h}^{-1}$) dominated the total production of OH (Fig. S3a). Meanwhile, OH-initiated oxidations of VOCs ($4.9 \pm 3.3 \text{ ppb h}^{-1}$) consumed OH most during the daytime, followed by $\text{OH} + \text{CO}$ ($2.6 \pm 1.9 \text{ ppb h}^{-1}$), $\text{OH} + \text{NO}_2$ ($2.4 \pm 1.1 \text{ ppb h}^{-1}$), $\text{OH} + \text{NO}$ ($0.6 \pm 0.3 \text{ ppb h}^{-1}$), and $\text{OH} + \text{O}_3$ ($0.2 \pm 0.1 \text{ ppb h}^{-1}$).

In this study, HCHO photolysis was identified as the most important source for HO_2 primary formation, with an average production rate of $1.1 \pm 0.6 \text{ ppb h}^{-1}$ (Fig. 6c), followed by the other OVOCs photolysis ($0.4 \pm 0.2 \text{ ppb h}^{-1}$). The rate of OVOCs photolysis in Xiamen was much lower than that in some megacities, such as Beijing (Liu et al., 2012) and Hong Kong (Xue et al., 2016). The reaction of $\text{OH} + \text{CO}$ ($2.6 \pm 2.2 \text{ ppb h}^{-1}$) and $\text{RO}_2 + \text{NO}$ ($2.5 \pm 1.5 \text{ ppb h}^{-1}$) were also important sources of HO_2 (Fig. S3b). The main sink of HO_2 was $\text{HO}_2 + \text{NO}$ ($7.9 \pm 6.2 \text{ ppb h}^{-1}$), while the loss rates of $\text{HO}_2 + \text{HO}_2$ and $\text{HO}_2 + \text{RO}_2$ were negligible.

In Fig. 6d, OVOCs photolysis contributed most to primary RO_2 production with a rate of $0.5 \pm 0.2 \text{ ppb h}^{-1}$, accounting for $85 \pm 20\%$ of total RO_2 primary production. The reaction of unsaturated VOCs and NO_3 was the second important source, accounting for $11 \pm 18\%$ of the total primary RO_2 . The radical recycling rate of $\text{OH} + \text{VOCs}$ was 8.4 times higher than the sum of RO_2 primary production. The consumption reaction of RO_2 was mainly caused by $\text{RO}_2 + \text{NO}$ ($3.7 \pm 2.9 \text{ ppb h}^{-1}$), and the cross-reactions by ROx themselves were limited.

The daytime average ROx budget and its recycling were also demonstrated (Fig. 7). For the ROx primary sources, the photolysis of HONO ($33 \pm 14\%$), O_3 ($25 \pm 13\%$), HCHO ($20 \pm 5\%$) and other OVOCs ($17 \pm 2\%$) were the major contributors. For ROx recycling, CO and VOCs reacted with OH producing HO_2 and RO_2 with the average rates of 4.0 and 4.4 ppbv h^{-1} , respectively. $\text{RO}_2 + \text{NO}$ and $\text{HO}_2 + \text{NO}$ enhanced the production of RO (3.6 ppbv h^{-1}) and OH (7.9 ppbv h^{-1}), with O_3 formed as a by-product. For the termination processes, the reaction rates of ROx and NOx were approximately 2-5 times faster than the cross-reaction rates of ROx .

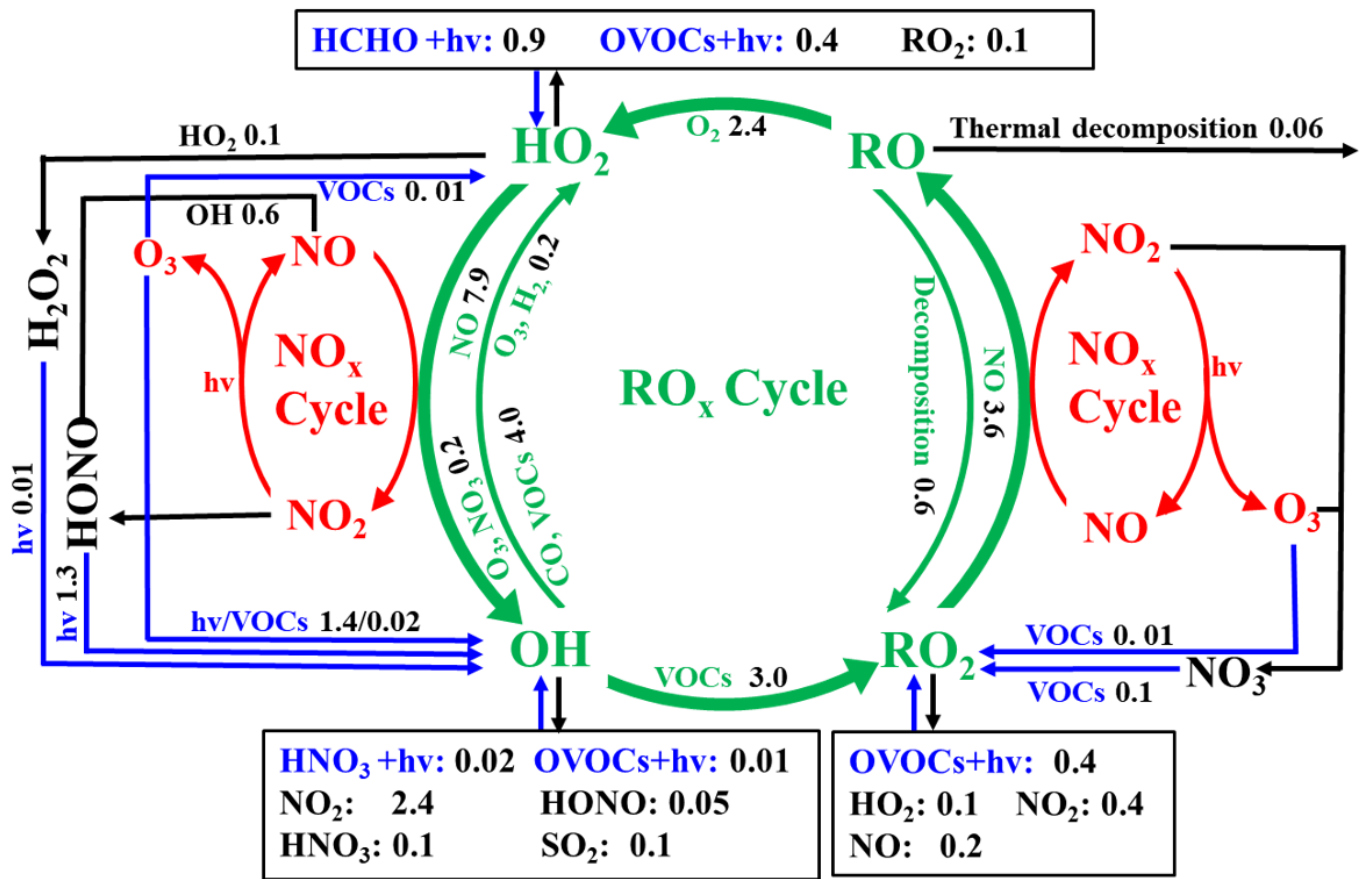


Figure 7. Daytime RO_x budget during 20-29 Sep. 2019 in Xiamen. The unit is parts per billion per hour. The blue, black, and green lines and words indicate the production, destruction, recycling pathways of radicals, respectively.

3.3 O₃ formation mechanism

3.3.1 Chemical budget and sensitivity analysis of O₃ production

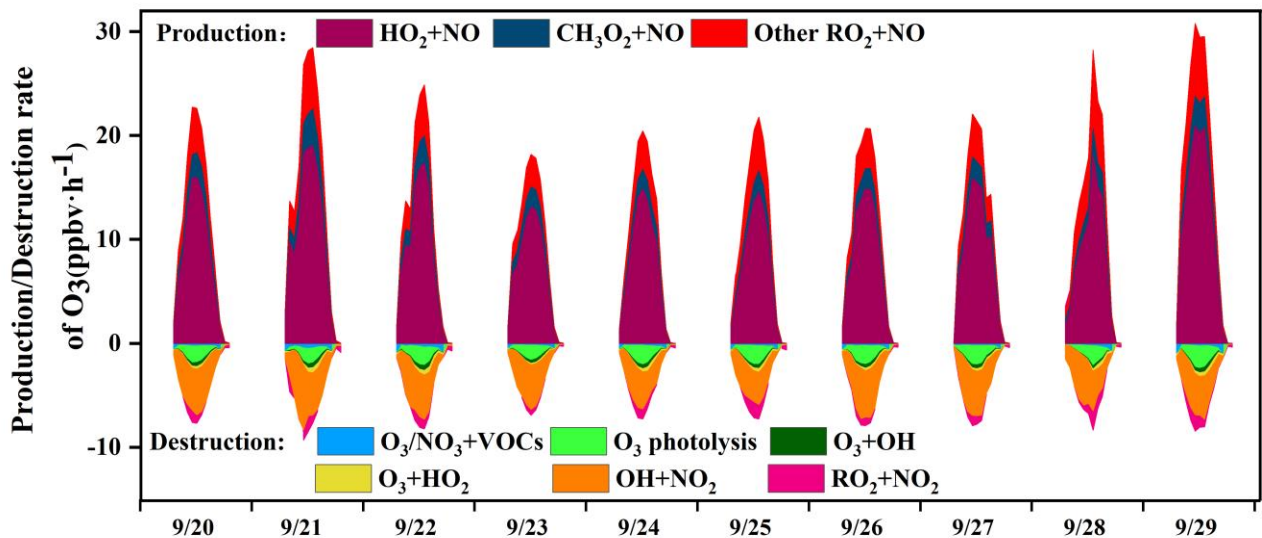


Figure 8. Time series of model-simulated O₃ chemical budgets during 20-29 Sep. 2019 in Xiamen.

The in situ O₃ production mechanism was examined, and the detailed reaction weights were shown

in Fig. 8. The daytime rate of HO_2+NO was $7.9\pm 6.2 \text{ ppb h}^{-1}$, accounting for $68\pm 4\%$ of the total O_3 production. This result was consistent with that in section 3.2.2. The OH radical was the initiator of O_3 photochemical formation, and the source of OH from HO_2+NO was also the dominant pathway to produce O_3 (Liu et al., 2020c). The second pathway of O_3 production was RO_2+NO ($3.6\pm 2.0 \text{ ppb h}^{-1}$). The reaction of RO_2+NO contained more than 1000 types of RO_2 radicals, and the pathway of $\text{CH}_3\text{O}_2+\text{NO}$ ($34\pm 6\%$) contributed mostly among them. In contrast, the contributors of O_3 destruction were $\text{OH}+\text{NO}_2$ ($61\pm 18\%$), followed by O_3 photolysis ($18\pm 9\%$), RO_2+NO_2 ($9\pm 10\%$), O_3+HO_2 ($4\pm 4\%$), and O_3+OH ($4\pm 2\%$), while the other pathways of O_3+VOCs as well as NO_3+VOCs contributed limitedly. In addition, the net O_3 production ($9.1\pm 5.7 \text{ ppb h}^{-1}$) in Xiamen was $\sim 2\text{-}5$ times lower than that derived from the metropolis of Shanghai (26 ppb h^{-1}), Lanzhou (23 ppb h^{-1}) and Guangzhou (50 ppb h^{-1}), reflecting the influence of O_3 precursor emissions and photochemical conditions (Xue et al., 2014).

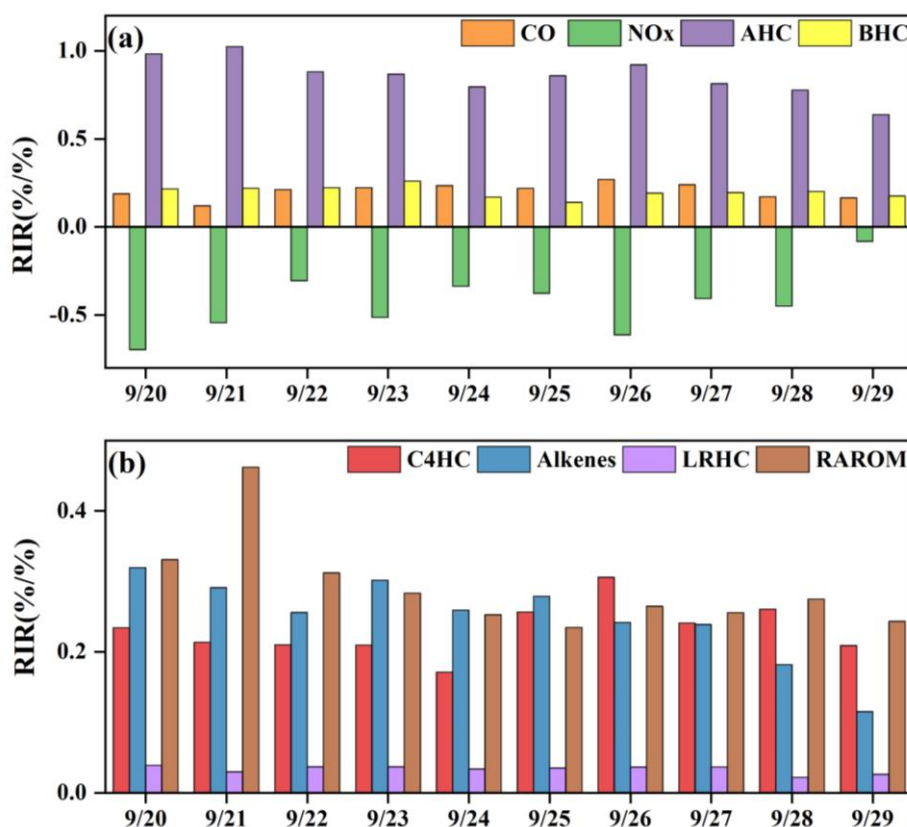
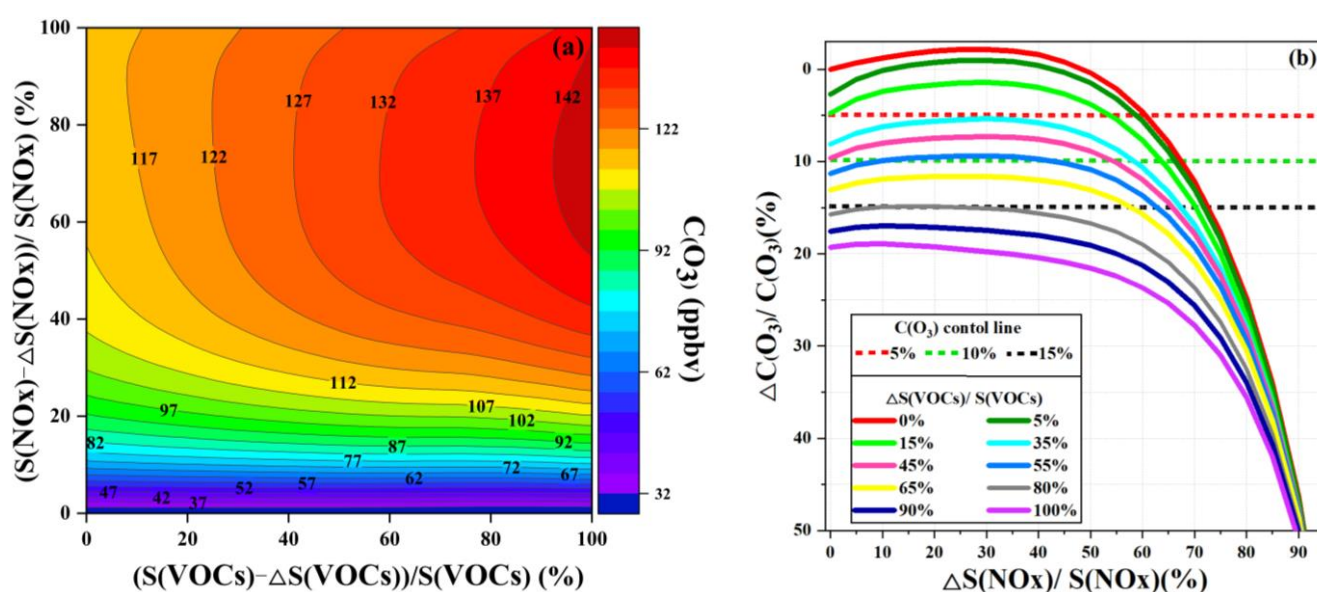


Figure 9. The model-calculated RIRs for (a) major O_3 precursor groups and (b) the AHC sub-groups during high O_3 daytime (06:00-18:00 LT) (AHC: anthropogenic hydrocarbons; BHC: biogenic hydrocarbons; RAROM: aromatics except for benzene; LRHC: low reactivity hydrocarbons; C4HC: alkenes, and alkanes with ≥ 4 carbons).

In this study, we also calculated the relative incremental reactivity (RIR) to diagnose the sensitivity of O_3 formation to its precursors. Figure 9 shows the RIR values for major groups of O_3 precursors. Around 50 types of VOCs were classified as anthropogenic hydrocarbons (AHC), and the isoprene was categorized into biogenic hydrocarbons (BHC). Moreover, AHC further divided into four groups of

399 reactive aromatics (RAROM, including aromatics except for benzene), low reactivity hydrocarbons
 400 (LRHC, including ethane, acetylene, propane, and benzene), alkenes, and alkanes with ≥ 4 carbons
 401 (C4HC). The in situ O_3 production was highly VOCs-sensitive, especially for AHC-sensitive
 402 (0.63–1.02 %/%) (Fig. 9a), followed by CO (0.17–0.27 %/%) and BHC (0.14–0.26 %/%), indicating the
 403 impacts from anthropogenic activities and flourishing vegetation emissions (Liu et al., 2020a; Lin et al.,
 404 2020). The RIRs were NO_x -negative ranging from -0.70 to -0.08. As shown in Fig. 9b, the contributors
 405 of AHC sub-groups to RIRs were RAROM (0.24–0.46 %/%), C4HC (0.17–0.30 %/%), alkenes
 406 (0.11–0.32 %/%), and LRHC (0.03–0.04 %/%). Therefore, the reduction of aromatics, alkenes, and
 407 alkanes with ≥ 4 carbons effectively decreased O_3 production, and the reduction of NO_x might aggravate
 408 O_3 pollution.



409
 410 **Figure 10. (a) Isopleth diagrams of modeled O_3 production potential ($C(O_3)$) on $S(VOCs)$ and $S(NO_x)$ remaining**
 411 **percentages (i.e., $(S(VOCs)-\Delta S(VOCs))/S(VOCs)$ and $(S(NO_x)-\Delta S(NO_x))/S(NO_x)$); (b) Relationship of $C(O_3)$**
 412 **increment percentage ($\Delta C(O_3)/C(O_3)$) with $S(NO_x)$ and $S(VOCs)$ reduction percentages ($\Delta S(NO_x)/S(NO_x)$ and**
 413 **$\Delta S(VOCs)/S(VOCs)$). Note: $C(O_3)$, $S(NO_x)$, and $S(NO_x)$ represent the concentrations of corresponding**
 414 **pollutants.**

415 In order to investigate the O_3 control strategies during this multi-day O_3 pollution event, the scenario
 416 analysis with reduction by 0-100% at intervals of 5% for the reduction of anthropogenic VOCs
 417 ($\Delta S(VOCs)/S(VOCs)$ and NO_x ($\Delta S(NO_x)/S(NO_x)$) were conducted using the OBM-MCM. According
 418 to the Empirical Kinetic Modeling Approach (EKMA) and scenario analysis, O_3 formation was in the
 419 NO-titration regime (Fig. 10), in accordance with those of RIR analysis, which meant VOCs should be
 420 reduced to effectively control O_3 during the O_3 pollution event. The maximum value of MDA8h O_3 during
 421 the monitoring period was 85 ppbv, exceeding the national air quality standard of 75 ppbv for O_3 by 13%.
 422 Hence, the O_3 reductions of 5%, 10%, and 15% were set to discuss the reduction schemes of

anthropogenic VOCs and NO_x. As shown in Fig. 10b, achieving the 5% control target were 1) S(VOCs) is reduced by 15%, while S(NO_x) remains unchanged; 2) S(VOCs) is reduced larger than 35%; 3) S(NO_x) reduction is higher than 60%. The first scenario of just reducing VOCs emission was the most cost-efficient way for short-term or emergency control of O₃. However, NO_x, as important precursors of PM_{2.5}, need to be reduced according to the long-term multi-pollutant control air quality improvement plan in China, thus the second scenario is a more practical and reasonable way to control air pollution. The 10% of O₃ control target was achieved by the 45% reduction of S(VOCs), and the S(NO_x) keeps original emission. In view of the long-term control strategy of NO_x and VOCs, S(VOCs) reduced by 55% and 80% could decrease 10% and 15% O₃ concentrations, respectively. Although VOCs and NO_x control measures were drastically implemented, it is still challenging to achieve the 15% O₃ control goals in urban areas with relatively low precursor emissions. As the episode is a typical pollution process in the coastal region, the research results might act as reference for the policy makers. Meanwhile, as the O₃ sensitivity changed under the implementation of control measures, it is necessary to adjust timely the reduction of VOC and NO_x policies.

3.3.2 O₃ from local photochemical production and regional transport

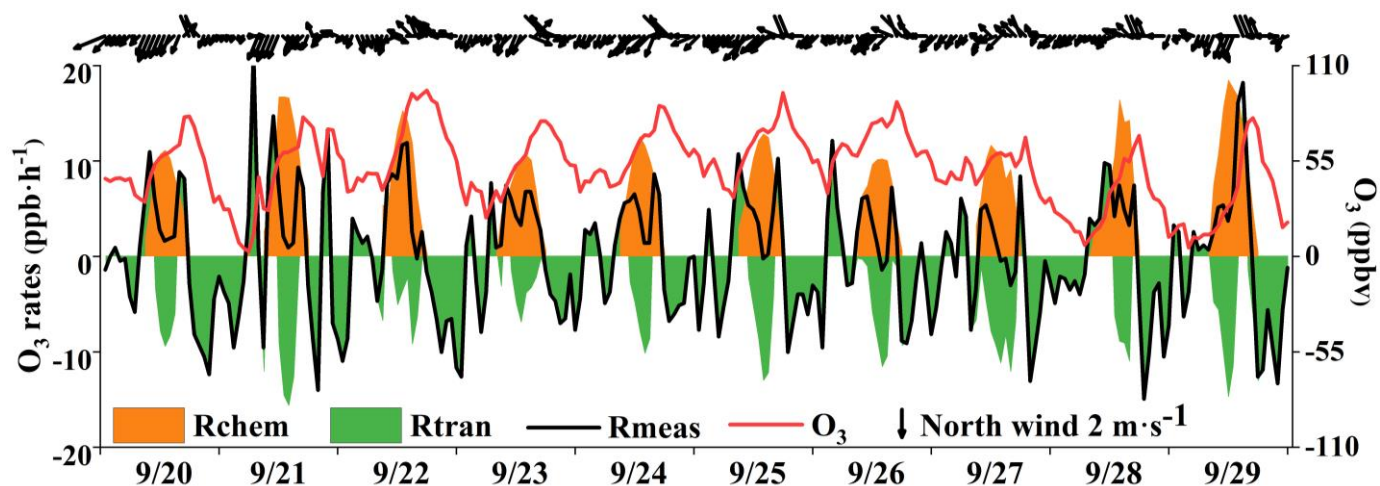


Figure 11. O₃ accumulation and contributions from local photochemical production and regional transport, and Rchem, Rtran, and Rmeas in figure caption represent local O₃ photochemical production, regional transport and observed O₃ formation rate, respectively.

Previous studies have found that the variation of O₃ mixing ratios was mainly influenced by chemical and physical processes (Xue et al., 2014; Tan et al., 2018). Figure 11 shows the time series of O₃ accumulation and contributions from local photochemical production and regional transport. The observed rate of change in O₃ (Rmeas) was calculated by the derivative of the observed O₃ concentrations ($R_{meas} = d(O_3)/dt$). The local O₃ production (Rchem) was calculated by Equation 3, and computed hourly by the OBM as described in Section 2.2. The physical processes (Rtran) were calculated by the equation

448 of $R_{\text{tran}} = R_{\text{meas}} - R_{\text{chem}}$, including horizontal and/or vertical transport, dry deposition dilution mixing,
449 and so on. Many studies showed that the impacts of dry deposition were minor, thus the differences
450 between observed O_3 changes and local O_3 production were mainly caused by the regional transport (note
451 that the effect of atmospheric mixing was also included in this term), which could be treated as regional
452 transport and could reasonably quantify the contributions of regional transport at our observation site
453 (Zhang et al., 2021; Chen et al., 2020). The positive values of R_{tran} represented the O_3 import of regional
454 transport, while the negative values indicated the O_3 export and deposition. We quantified the
455 contributions of local photochemical formation and regional transport to the observed O_3 , and figured out
456 the reasons for the O_3 pollution process.

457 As shown in Fig. 11, two regular O_3 import phenomenon with positive values of R_{tran} were observed,
458 and the curve of the R_{meas} showed the “M” trend during the daytime. The first transient intense O_3 import
459 happened in the early morning (at around 6:00-9:00), leading to a rapid increase in O_3 concentration,
460 which was mainly attributed to the residual ozone from the day before. The O_3 export was remarkable at
461 around 10:00-16:00, indicating the potential impacts on air quality in downwind areas. Generally, the
462 maximum daily value of O_3 at this observation site appeared at around 15:00 LT without regional transport
463 (Wu et al., 2019). In Figure 11, we found that the O_3 concentrations showed two peaks at around 15:00
464 and 17:00 LT, and O_3 concentrations rose slowly, or even decreased firstly and then increased between
465 the two peaks. Under these circumstances, the local photochemical production kept producing O_3 , but the
466 decreased O_3 concentrations could be attributed to the favorable atmospheric conditions in diluting
467 pollutants (O_3 export). When the near-surface wind direction changed from northeast to southeast, the
468 second O_3 import phenomenon occurred in the afternoon (16:00-19:00 LT) in four days (20, 25 27 and 29
469 Sep.). Due to the persistence of R_{tran} in the afternoon, the daily maximum O_3 values appeared at around
470 17:00 LT. Under the conditions of southeast wind direction, downtown area with high density vehicles
471 would make O_3 and its precursors transmitting to our observation site, consistent with the diurnal patterns
472 of NO_2 , OVOCs, alkanes, and aromatic in the early morning and afternoon (Fig. 2) to match with the “M”
473 trend of R_{meas} . This result indicated that the sudden changes of near-surface winds were corresponding
474 to the variation in the transport of the urban plume.

475 According to the synoptic situations and meteorological parameters (Fig. 1, Fig. S4 and Fig.12), the
476 environmental conditions also favored the O_3 pollution process during the observation periods. The
477 contribution of R_{chem} (daily maximum: ranged from 10.2 to 19.1 ppb h^{-1}) during the daytime was
478 observed (Fig.11). In Fig. S4abc, the monitoring site was continuously affected by the northerly airflow

479 with high O₃ and its precursors (from an industrial city adjacent to Xiamen of Quanzhou or polluted
 480 regions of Yangtze River Delta), due to the typhoon ‘Tapah’ from 20 to 22 Sep. 2019. The transport of O₃
 481 import appeared on 21 Sep. (7.1 ± 7.0 ppb h⁻¹), which resulted in the accumulation of O₃ (the MDA8h O₃:
 482 85 ppbv) on 22 Sep. When the influence of typhoon disappeared, the direction of airflow turned from
 483 northerly into southwest with humid and warm at 500hPa (Fig. S4d), the surface wind on Sep. 23 was
 484 affected by the control of the cold northerly airflow (Fig. S4ef). Meteorological conditions including
 485 continental high pressure during 23 to 27 Sep. were favorable to the accumulation of air pollutants (Fig.
 486 12). The isoline of 5880 gpm moving from north to the Yangtze River (Fig. 12a,b) indicated the
 487 strengthened subtropical high pressure during 23-27 Sep. 2019, which carried high temperature, low RH,
 488 and stagnant weather conditions, and the transport rate of O₃ export (5.4 ± 3.4 ppb h⁻¹) on 24-26 Sep. was
 489 lower than that on other days (6.3 ± 4.0 ppb h⁻¹). Favorable meteorological conditions significantly
 490 affected the formation and accumulation of O₃, and we chose five meteorological parameters (i.e. UV, T,
 491 RH, P and WS) to quantify the complex nonlinear relationships between O₃ and its influencing factors
 492 based on a generalized additive model (GAM) (Hua et al., 2021). Table S3 showed that the factors had
 493 significant non-linear impacts on O₃ concentration changes at the level of P-value<0.01 and degrees of
 494 freedom>1, indicating that each influencing factor has statistical significance as an explanatory variable.
 495 According to the F-values reflecting the importance of the influencing factors, the orders of the
 496 explanatory variables were RH (40.1) > WS (26.9) > T (10.9) > P (3.9) > UV (3.0). Response curves of
 497 O₃ concentration to explanatory factors are presented in Fig. 13. The O₃ concentration showed a
 498 remarkable upward trend until the UV increased to 17 W·m⁻², then changed little with the fluctuation of
 499 UV (Fig. 13a). In previous studies, UV had a significant positive correlation with O₃ concentrations (Ma
 500 et al., 2020), and these results showed the regional transport impacts on O₃ formation in our study. The
 501 RH and T had negative and positive correlations with O₃ concentrations, respectively (Fig. 13b and Fig.
 502 13c). The increase of wind speed was favorable for O₃ regional transport (Fig. 13d). The influence of
 503 atmospheric pressure on O₃ seemed to be irregular and minor, which could be ignored (Fig. 13e). Hence,
 504 under the combined effects of favorable photochemical reaction conditions and strengthened WPSH, the
 505 MDA8h O₃ exceeded the standard of 75 ppbv during 24-26 Sep. Previous studies had found that severe
 506 multi-day O₃ pollution appeared under the WPSH control (Wang et al., 2018a). Overall, the results
 507 indicate that the three conditions of local photochemical production, synoptic situations and regional
 508 transport played very important roles in the pollution event.

509

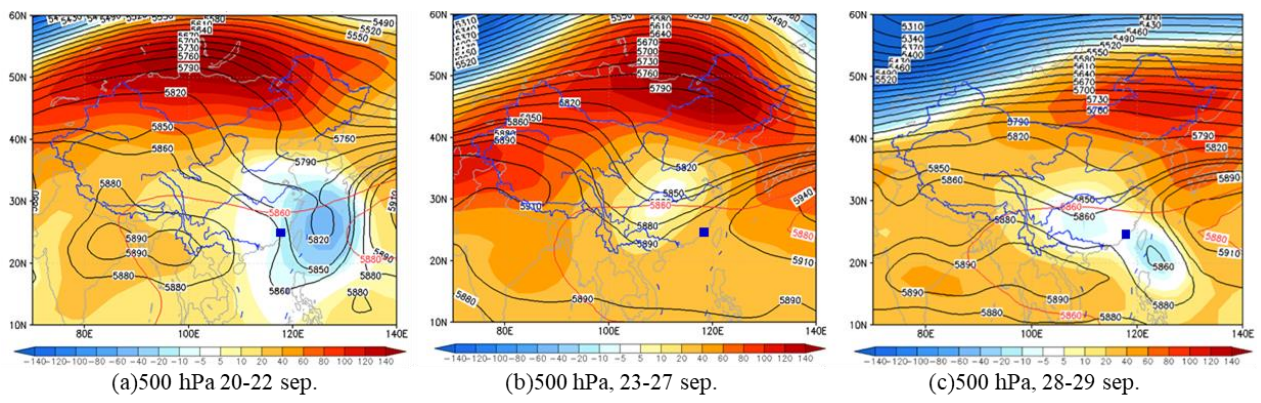


Figure 12. Synoptic situations of continental high pressure from 20 to 29 Sep. 2019. The gradient color area indicates the WPSH over the map and the contour line was from the characteristic isoline of 5880 gpm to the center isoline of 5920 gpm. The blue square is the study site.

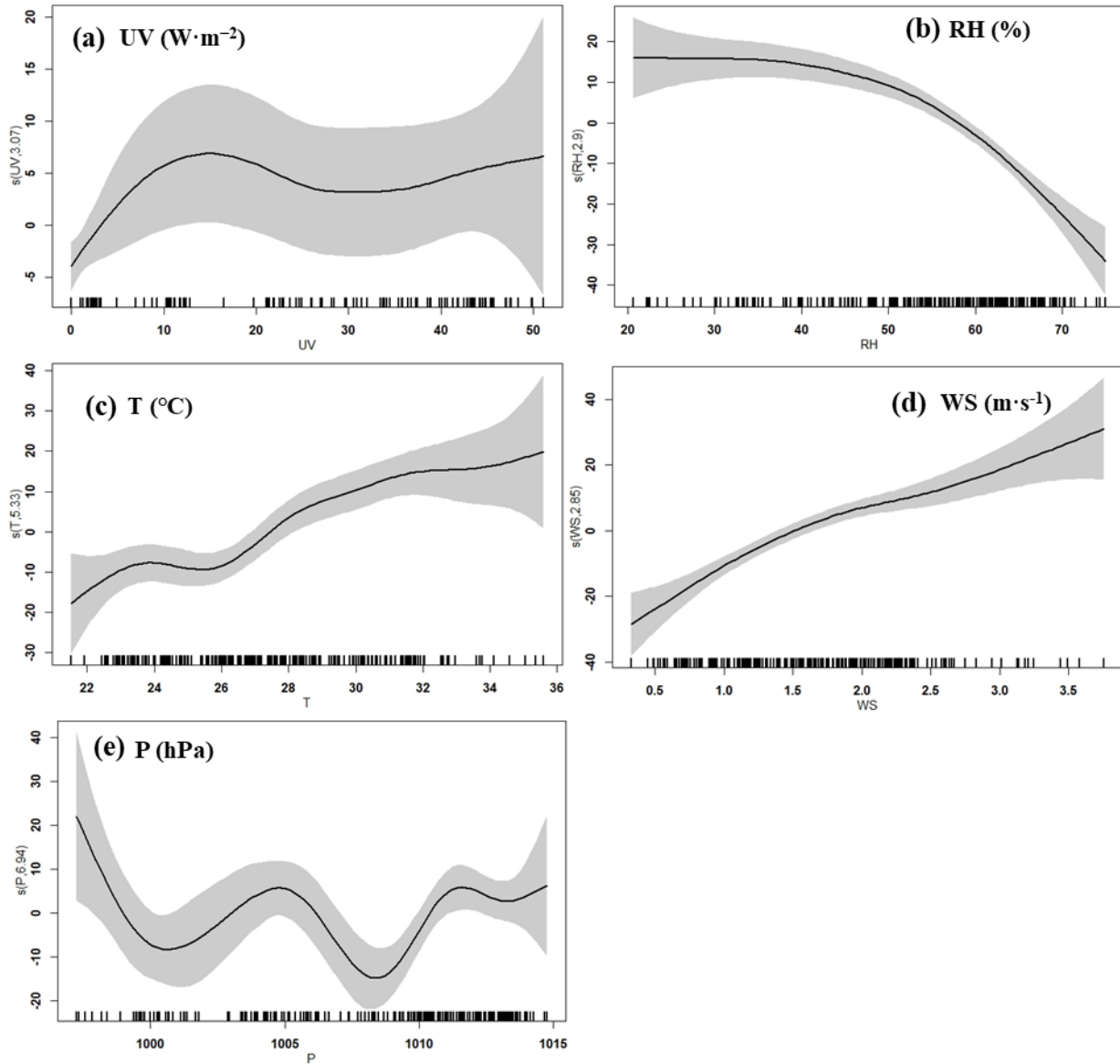


Figure 13. Response curves in GAM model of O_3 concentration to changes in (a) ultraviolet radiation (UV), (b) relative humidity (RH), (c) temperature (T), (d) wind speed (WS), and (e) pressure (P). The y-axis is the smoothing function values. The x-axis is the influencing factor; the vertical short lines represent the concentration distribution characteristics of the explanatory variables; the shaded area around the solid line indicates the 95%

confidence interval of O₃ concentration.

4 Conclusions

In the present study, we analyzed a typical high O₃ event during 20-29 Sep. 2019 in a coastal city of Southeast China. We clarified the characteristics of AOC, OH reactivity, and radical chemistry, as well as O₃ formation mechanisms using the OBM-MCM model. The predominant oxidant for AOC during the daytime and nighttime was the OH and NO₃, respectively. During the period of O₃ pollution process, OVOCs, NO₂, and CO consumed OH mostly. Meanwhile, the photolysis of HONO, O₃, HCHO, and other OVOCs were major sources of RO_x, which played the initiation roles in atmospheric oxidation processes. The radical termination reactions were governed by cross-reactions between RO_x and NO_x. The RIRs and EKMA results showed that the O₃ formation in autumn in the coastal city was VOCs-sensitive, and the VOCs were the limited factor of radical recycling and O₃ formation. The reduced emissions of aromatics, alkenes, and alkanes with ≥ 4 carbons were benefit for ozone pollution control. The three conditions of local photochemical production, synoptic situations and regional transport played very important roles in the pollution event. Overall, the results clarified the O₃ pollution process with relatively low local precursor emissions, and implied the fact that O₃ pollution control in coastal cities needs to be further studied.

Code/Data availability

The observation data at this site are available from the authors upon request.

Authorship Contribution Statement

Taotao Liu and Youwei Hong contributed equally to this work. Jinsheng Chen and Likun Xue designed and revised the manuscript. Taotao Liu collected the data, contributed to the data analysis. Taotao Liu and Youwei Hong performed chemical modeling analyses of OBM-MCM and wrote the paper. Jinsheng Chen supported funding of observation and research. Lingling Xu, Mengren Li, Chen Yang, Yangbin Dan, Yingnan Zhang, and Min Zhao contributed to discussions of results. Zhi Huang and Hong Wang provided meteorological conditions in Xiamen.

Competing interests

The authors declare that they have no conflict of interest.

551

552 **Acknowledgments**

553 This study was funded by the Cultivating Project of Strategic Priority Research Program of Chinese
 554 Academy of Sciences (XDPB1903), the FJIRSM&IUE Joint Research Fund (RHZX-2019-006), the
 555 Center for Excellence in Regional Atmospheric Environment, CAS (E0L1B20201), the Xiamen Youth
 556 Innovation Fund Project (3502Z20206094), the foreign cooperation project of Fujian Province
 557 (2020I0038) and Xiamen Atmospheric Environment Observation and Research Station of Fujian Province.

558

559 **Supplementary information**

560 Attached please find supplementary information associated with this article.

561

562 **References:**

- 563 Acker, K., Möller, D., Wieprecht, W., Auel, R., Kalaß, D., and Tschewenka, W.: Nitrous and nitric acid
 564 measurements inside and outside of clouds at Mt. Brocken, *Water Air Soil Pollut.*, 130, 331–336, 2001.
- 565 Chang, L., Xu, J., Tie, X., and Gao, W.: The impact of Climate Change on the Western Pacific Subtropical High
 566 and the related ozone pollution in Shanghai, China, *Sci Rep*, 9, 16998, 10.1038/s41598-019-53103-7, 2019.
- 567 Chen, T., Xue, L., Zheng, P., Zhang, Y., Liu, Y., Sun, J., Han, G., Li, H., Zhang, X., Li, Y., Li, H., Dong, C., Xu, F.,
 568 Zhang, Q., and Wang, W.: Volatile organic compounds and ozone air pollution in an oil production region in
 569 northern China, *Atmos. Chem. Phys.*, 20, 7069-7086, 10.5194/acp-20-7069-2020, 2020.
- 570 Deng, J., Guo, H., Zhang, H., Zhu, J., Wang, X., and Fu, P.: Source apportionment of black carbon aerosols from
 571 light absorption observation and source-oriented modeling: an implication in a coastal city in China, *Atmospheric
 572 Chemistry and Physics*, 20, 14419-14435, 10.5194/acp-20-14419-2020, 2020.
- 573 Edwards, P. M., Brown, S. S., Roberts, J. M., Ahmadov, R., Banta, R. M., Degouw, J. A., Dubé, W. P., Field, R. A.,
 574 Flynn, J. H., Gilman, J. B., and Graus, M.: High winter ozone pollution from carbonyl photolysis in an oil and gas
 575 basin, *Nature*, 514, 351, <https://doi.org/10.1038/nature13767>, 2014.
- 576 Edwards, P. M., Young, C. J., Aikin, K., deGouw, J., Dubé, W. P., Geiger, F., Gilman, J., Helmig, D., Holloway, J.
 577 S., Kercher, J., Lerner, B., Martin, R., McLaren, R., Parrish, D. D., Peischl, J., Roberts, J. M., Ryerson, T. B.,
 578 Thornton, J., Warneke, C., Williams, E. J., and Brown, S. S.: Ozone photochemistry in an oil and natural gas
 579 extraction region during winter: simulations of a snow-free season in the Uintah Basin, Utah, *Atmos. Chem. Phys.*,
 580 13, 8955–8971, <https://doi.org/10.5194/acp13-8955-2013>, 2013.
- 581 Eisele, F. L., Mount, G. H., Tanner, D., Jefferson, A., Shetter, R., Harder, J. W., and Williams, E. J.: Understanding
 582 the production and interconversion of the hydroxyl radical during the Tropospheric OH Photochemistry Experiment,
 583 *J. Geophys. Res.*, 102, 6457–6465, 1997.
- 584 Elshorbany, Y. F., Kurtenbach, R., Wiesen, P., Lissi, E., Rubio, M., Villena, G., Gramsch, E., Rickard, A. R., Pilling,
 585 M. J., and Kleffmann, J.: Oxidation capacity of the city air of Santiago, Chile, *Atmos. Chem. Phys.*, 9, 2257–2273,

586 <https://doi.org/10.5194/acp-9-2257-2009>, 2009.

587 Emmerson, K. M., Carslaw, N., and Pilling, M. J.: Urban Atmospheric Chemistry During the PUMA Campaign 2:
 588 Radical Budgets for OH, HO₂ and RO₂, *J. Atmos. Chem.*, 52, 165-183, 10.1007/s10874-005-1323-2, 2005.

589 Fowler, D., Pilegaard, K., Sutton, M. A., Ambus, P., Raivonen, M., Duyzer, J., Simpson, D., Fagerli, H., Fuzzi, S.,
 590 Schjoerring, J. K., Granier, C., Neftel, A., Isaksen, I. S. A., Laj, P., Maione, M., Monks, P. S., Burkhardt, J.,
 591 Daemmgen, U., Neirynck, J., Personne, E., Wichink-Kruit, R., Butterbach-Bahl, K., Flechard, C., Tuovinen, J. P.,
 592 Coyle, M., Gerosa, G., Loubet, B., Altimir, N., Gruenhage, L., Ammann, C., Cieslik, S., Paoletti, E., Mikkelsen, T.
 593 N., Ro-Poulsen, H., Cellier, P., Cape, J. N., Horváth, L., Loreto, F., Niinemets, Ü., Palmer, P. I., Rinne, J., Misztal,
 594 P., Nemitz, E., Nilsson, D., Pryor, S., Gallagher, M. W., Vesala, T., Skiba, U., Brüggemann, N., Zechmeister-
 595 Boltenstern, S., Williams, J., O'Dowd, C., Facchini, M. C., de Leeuw, G., Flossman, A., Chaumerliac, N., and
 596 Erisman, J. W.: Atmospheric composition change: Ecosystems–Atmosphere interactions, *Atmos. Environ.*, 43,
 597 5193-5267, 10.1016/j.atmosenv.2009.07.068, 2009.

598 George, L. A., Hard, T. M., and O'Brien, R. J.: Measurement of free radicals OH and HO₂ in Los Angeles smog, *J.*
 599 *Geophys. Res.*, 104, 11643–11655, 1999.

600 Geyer, A., Alicke, B., Konrad, S., Schmitz, T., Stutz, J., and Platt, U.: Chemistry and oxidation capacity of the
 601 nitrate radical in the continental boundary layer near Berlin, *J. Geophys. Res.*, 106, 8013-8025,
 602 10.1029/2000jd900681, 2001.

603 Gong, C., and Liao, H.: A typical weather pattern for the ozone pollution events in North China, *Atmos. Chem.*
 604 *Phys.*, 10.5194/acp-2019-263, 2019.

605 Hofzumahaus, A., Rohrer, F., Lu, K. D., Bohn, B., Brauers, T., Chang, C. C., Fuchs, H., Holland, F., Kita, K.,
 606 Kondo, Y., Li, X., Lou, S. R., Shao, M., Zeng, L. M., Wahner, A., and Zhang, Y. H.: Amplified Trace Gas Removal
 607 in the Troposphere, *Science*, 324, 1702–1704, 2009.

608 Hong, Z., MengzeLi, HongWang, LinglingXu, Hong, Y., Chen, J., Chen, J., Zhang, H., Zhang, Y., Wu, X., Hu, B.,
 609 and Li, M.: Characteristics of atmospheric volatile organic compounds (VOCs) at a mountainous forest site and
 610 two urban sites in the southeast of China, *Sci Total Environ*, 10.1016/j.scitotenv.2018.12.132, 2019.

611 Hu B, Liu T, Yang Y, Hong Y, Li M, Xu L, Wang H, Chen N, Wu X, Chen J: Characteristics and Formation
 612 Mechanism of Surface Ozone in a Coastal Island of Southeast China: Influence of Sea-land Breezes and Regional
 613 Transport. *Aerosol Air Qual. Res.*, 19(8):1734-1748, 2019.

614 Hu, B., Duan, J., Hong, Y., Xu, L., Li, M., Bian, Y., Qin, M., Fang, W., Xie, P., and Chen, J.: Exploration of the
 615 atmospheric chemistry of nitrous acid in a coastal city of southeastern China: Results from measurements across
 616 four seasons, *Atmos. Chem. Phys. Discuss.* [preprint], <https://doi.org/10.5194/acp-2021-723>, 2021.

617 Hu, B., Liu, T., Hong, Y., Xu, L., Li, M., Wu, X., Wang, H., Chen, J., and Chen, J.: Characteristics of peroxyacetyl
 618 nitrate (PAN) in a coastal city of southeastern China: Photochemical mechanism and pollution process, *Sci Total*
 619 *Environ*, 719, 137493, 10.1016/j.scitotenv.2020.137493, 2020.

620 Hansen R F, Griffith S M, Dusanter S, et al.: Measurements of Total OH Reactivity During CalNex-LA. *J. Geophys.*
 621 *Res, Atmos*, 126(11), e2020JD032988, 2021.

622 Jenkin, M. E., Saunders, S. M., Wagner, V., and Pilling, M. J.: Protocol for the development of the Master Chemical
 623 Mechanism, MCM v3 (Part B): tropospheric degradation of aromatic volatile organic compounds, *Atmos. Chem.*
 624 *Phys.*, 3, 181–193, <https://doi.org/10.5194/acp-3-181-2003>, 2003.

625 Hansen R F, Griffith S M, Dusanter S, et al.: Measurements of Total OH Reactivity During CalNex-LA.
 626 *J. Geophys. Res, Atmos*, 126(11), e2020JD032988, 2021.

627 Hua, J., Zhang, Y., de Foy, B., Shang, J., Schauer, J. J., Mei, X., Sulaymon, I. D., and Han, T.: Quantitative
628 estimation of meteorological impacts and the COVID-19 lockdown reductions on NO₂ and PM_{2.5} over the Beijing
629 area using Generalized Additive Models (GAM), *J Environ Manage*, 291, 112676, 10.1016/j.jenvman.2021.112676,
630 2021.

631 Jiang Y, Xue L, Gu R, Jia M, Zhang Y, Wen L, Zheng P, Chen T, Li H, Shan Y et al: Sources of nitrous acid (HONO)
632 in the upper boundary layer and lower free troposphere of the North China Plain: insights from the Mount Tai
633 Observatory. *Atmos. Chem. Phys.*, 20(20):12115-12131, 2020.

634 Kanaya, Y., Cao, R. Q., Akimoto, H., Fukuda, M., Komazaki, Y., Yokouchi, Y., Koike, M., Tanimoto, H., Takegawa,
635 N., and Kondo, Y.: Urban photochemistry in central Tokyo: 1. Observed and modeled OH and HO₂ radical
636 concentrations during the winter and summer of 2004, *J. Geophys. Res.*, 112, D21312, doi:10.1029/2007JD008670,
637 2007.

638 Kanaya, Y., Matsumoto, J., Kato, S., and Akimoto, H.: Behavior of OH and HO₂ radicals during the Observations
639 at a Remote Island of Okinawa (ORION99) field campaign 2. Comparison between observations and calculations,
640 *J. Geophys. Res.*, 106, 24209–24223, 2001.

641 Kovacs, T. A., Brune, W. H., Harder, H., Martinez, M., Simpas, J. B., Frost, G. J., Williams, E., Jobson, T., Stroud,
642 C., Young, V., Fried, A., and Wert, B.: Direct measurements of urban OH reactivity during Nashville SOS in
643 summer 1999, *J. of Environ. Monitor.*, 5, 68-74, 10.1039/b204339d, 2003.

644 Li, B., Ho, S. S. H., Gong, S., Ni, J., Li, H., Han, L., Yang, Y., Qi, Y., and Zhao, D.: Characterization of VOCs and
645 their related atmospheric processes in a central Chinese city during severe ozone pollution periods, *Atmos. Chem.*
646 *Phys.*, 19, 617-638, 10.5194/acp-19-617-2019, 2019.

647 Li, N., He, Q., Greenberg, J., Guenther, A., Cao, J., & Wang, J., Liao H., Zhang Q.: Impacts of biogenic and
648 anthropogenic emissions on summertime ozone formation in the Guanzhong Basin, China, *Atmos. Chem. Phys.*,
649 2018a.

650 Li, Z., Xue, L., Yang, X., Zha, Q., Tham, Y. J., Yan, C., Louie, P. K. K., Luk, C. W. Y., Wang, T., and Wang, W.:
651 Oxidizing capacity of the rural atmosphere in Hong Kong, Southern China, *Sci Total Environ*, 612, 1114-1122,
652 10.1016/j.scitotenv.2017.08.310, 2018.

653 Lin, H., Wang, M., Duan, Y., Fu, Q., Ji, W., Cui, H., Jin, D., Lin, Y., and Hu, K.: O₃ Sensitivity and Contributions
654 of Different NMHC Sources in O₃ Formation at Urban and Suburban Sites in Shanghai, *Atmosphere*, 11, 295,
655 10.3390/atmos 11030295, 2020.

656 Ling, Z., Zhao, J., Fan, S., and Wang, X.: Sources of formaldehyde and their contributions to photochemical O₃
657 formation at an urban site in the Pearl River Delta, southern China, *Chemosphere*, 168, 1293-1301,
658 10.1016/j.chemosphere. 2016.11.140, 2017.

659 Liu, J., Wang, L., Li, M., Liao, Z., Sun, Y., Song, T., Gao, W., Wang, Y., Li, Y., Ji, D., Hu, B., Kerminen, V.-M.,
660 Wang, Y., and Kulmala, M.: Quantifying the impact of synoptic circulation patterns on ozone variability in northern
661 China from April to October 2013Ó2017, *Atmos. Chem. Phys.*, 19, 14477-14492, 10.5194/acp-19-
662 14477-2019, 2019a.

663 Liu, T., Hu, B., Xu, X., Hong, Y., Zhang, Y., Wu, X., Xu, L., Li, M., Chen, Y., Chen, X., and Chen, J.: Characteristics
664 of PM_{2.5}-bound secondary organic aerosol tracers in a coastal city in Southeastern China: Seasonal patterns and
665 pollution identification, *Atmos. Environ.*, 237, 117710, 10.1016/j.atmosenv. 2020.117710, 2020a.

666 Liu, T., Hu, B., Yang, Y., Li, M., Hong, Y., Xu, X., Xu, L., Chen, N., Chen, Y., Xiao, H., and Chen, J.: Characteristics
667 and source apportionment of PM_{2.5} on an island in Southeast China: Impact of sea-salt and monsoon, *Atmos. Res.*,

235, 104786, 10.1016/j.atmosres.2019.104786, 2020b.

Liu, X., Lyu, X., Wang, Y., Jiang, F., and Guo, H.: Intercomparison of O₃ formation and radical chemistry in the past decade at a suburban site in Hong Kong, *Atmos. Chem. Phys.*, 19, 5127-5145, 10.5194/acp-19-5127-2019, 2019b.

Liu, X., Wang, N., Lyu, X., Zeren, Y., Jiang, F., Wang, X., Zou, S., Ling, Z., and Guo, H.: Photochemistry of ozone pollution in autumn in Pearl River Estuary, South China, *Sci Total Environ*, 754, 141812, 10.1016/j.scitotenv.2020.141812, 2020c.

Liu, Z., Wang, Y., Gu, D., Zhao, C., Huey, L., Stickel, R., Liao, J., Shao, M., Zhu, T., Zeng, L., Amoroso, A., Costabile, F., Chang, C., and Liu, S.: Summertime photochemistry during CARE Beijing-2007: RO₂ budgets and O₃ formation, *Atmos. Chem. Phys.*, 12, 7737-7752, 10.5194/acp-12-7737-2012, 2012.

Lou, S., Holland, F., Rohrer, F., Lu, K., Bohn, B., Brauers, T., Chang, C. C., Fuchs, H., Haeseler, R., Kita, K., Kondo, Y., Li, X., Shao, M., Zeng, L., Wahner, A., Zhang, Y., Wang, W., and Hofzumahaus, A.: Atmospheric OH reactivities in the Pearl River Delta - China in summer 2006: measurement and model results, *Atmos. Chem. Phys.*, 10, 11243-11260, 10.5194/acp-10-11243-2010, 2010a.

Lou, S., Holland, F., Rohrer, F., Lu, K., Bohn, B., Brauers, T., Chang, C., Fuchs, H., Häsel, R., Kita, K., Kondo, Y., Li, X., Shao, M., Zeng, L., Wahner, A., Zhang, Y., Wang, W., and Hofzumahaus, A.: Atmospheric OH reactivities in the Pearl River Delta – China in summer 2006: measurement and model results, *Atmos. Chem. Phys.*, 10, 11243-11260, 10.5194/acp-10-11243-2010, 2010b.

Lu, X., Hong, J., Zhang, L., Copper, O. R., Schultz, M. G., Xu, X., Wang, T., Gao, M., Zhao, Y., Zhang, Y. Severe Surface Ozone Pollution in China: A Global Perspective. *Environ. Sci. Technol. Lett.*, 5, 487-494, 2018.

Mao, J., Ren, X., Chen, S., Brune, W. H., Chen, Z., Martinez, M., Harder, H., Lefer, B., Rappenglück, B., Flynn, J., and Leuchner, M.: Atmospheric oxidation capacity in the summer of Houston 2006: Comparison with summer measurements in other metropolitan studies, *Atmos. Environ.*, 44, 4107-4115, 10.1016/j.atmosenv.2009.01.013, 2010.

Ma, Y., Ma, B., Jiao, H., Zhang, Y., Xin, J., and Yu, Z.: An analysis of the effects of weather and air pollution on tropospheric ozone using a generalized additive model in Western China: Lanzhou, Gansu, *Atmos. Environ.*, 224, 117342, 10.1016/j.atmosenv.2020.117342, 2020.

Martinez, M.: OH and HO₂ concentrations, sources, and loss rates during the Southern Oxidants Study in Nashville, Tennessee, summer 1999, *J. Geophys. Res.*, 108, 10.1029/2003jd003551, 2003.

Mazuza, G. M., Ren, X., Loughner, C.P., Estes, M., Crawford, J. H., Pickering, K. E., Weinheimer, A. J., Dickerson, R. R.: Ozone production and its sensitivity to NO_x and VOCs: results from the DISCOVER-AQ field experiment, Houston 2013. *Atmos. Chem. Phys.* 16, 14463–14474, 2016.

Michoud, V., Kukui, A., Camredon, M., Colomb, A., Borbon, A., Miet, K., Aumont, B., Beekmann, M., Durand-Jolibois, R., Perrier, S., Zapf, P., Siour, G., Ait-Helal, W., Locoge, N., Sauvage, S., Afif, C., Gros, V., Furger, M., Ancellet, G., and Doussin, J. F.: Radical budget analysis in a suburban European site during the MEGAPOLI summer field campaign, *Atmos. Chem. Phys.*, 12, 11951-11974, 10.5194/acp-12-11951-2012, 2012.

Nakashima Y , Kato S , Greenberg J , et al.: Total OH reactivity measurements in ambient air in a southern Rocky mountain ponderosa pine forest during BEACHON-SRM08 summer campaign[J]. *Atmos. Environ.*, 85(MAR.), 1-8, 2014.

Ren, X., Brune, W. H., Cantrell, C. A., Edwards, G. D., Shirley, T., Metcalf, A. R., and Lesh, R. L.: Hydroxyl and

peroxy radical chemistry in a rural area of Central Pennsylvania: Observations and model comparisons, *J. Atmos. Chem.*, 52, 231-257, 10.1007/s10874-005-3651-7, 2005.

Rollins, A. W., Browne, E. C., Min, K. E., Pusede, S. E., Wooldridge, P. J., Gentner, D. R., Goldstein, A. H., Liu, S., Day, D. A., Russell, L. M., and Cohen, R. C.: Evidence for NO_x Control over Nighttime SOA Formation, *Science*, 337, 1210–1212, 2012.

Saunders, S. M., Jenkin, M. E., Derwent, R. G., and Pilling, M. J.: Protocol for the development of the Master Chemical Mechanism, MCM v3 (Part A): tropospheric degradation of nonaromatic volatile organic compounds, *Atmos. Chem. Phys.*, 3, 161–180, doi:10.5194/acp-3-161-2003, 2003.

Sheehy, P. M., Volkamer, R., Molina, L. T., and Molina, M. J.: Oxidative capacity of the Mexico City atmosphere – Part 2: A RO₂ radical cycling perspective, *Atmos. Chem. Phys.*, 10, 6993-7008, 10.5194/acp-10-6993-2010, 2010.

Simon, H., Reff, A., Wells, B., Xing, J., and Frank, N.: Ozone trends across the United States over a period of decreasing NO_x and VOC emissions, *Environ. Sci. Technol.*, 49, 186-195, 10.1021/es504514z, 2015.

Smith, S. C., Lee, J. D., Bloss, W. J., Johnson, G. P., Ingham, T., and Heard, D. E.: Concentrations of OH and HO₂ radicals during NAMBLEX: measurements and steady state analysis, *Atmos. Chem. Phys.*, 6, 1435–1453, doi:10.5194/acp-6-1435-2006, 2006.

Tan, Z., Lu, K., Jiang, M., Su, R., Dong, H., Zeng, L., Xie, S., Tan, Q., and Zhang, Y.: Exploring ozone pollution in Chengdu, southwestern China: A case study from radical chemistry to O₃-VOC-NO_x sensitivity, *Sci Total Environ*, 636, 775-786, 10.1016/j.scitotenv.2018.04.286, 2018.

Tan, Z., Lu, K., Jiang, M., Su, R., Wang, H., Lou, S., Fu, Q., Zhai, C., Tan, Q., Yue, D., Chen, D., Wang, Z., Xie, S., Zeng, L., and Zhang, Y.: Daytime atmospheric oxidation capacity in four Chinese megacities during the photochemically polluted season: a case study based on box model simulation, *Atmos. Chem. Phys.*, 19, 3493-3513, 10.5194/acp-19-3493-2019, 2019.

Volkamer, R., Sheehy, P., Molina, L. T., and Molina, M. J.: Oxidative capacity of the Mexico City atmosphere – Part 1: A radical source perspective, *Atmos. Chem. Phys.*, 10, 6969-6991, 10.5194/acp-10-6969-2010, 2010.

Wang, H., Lyu, X., Guo, H., Wang, Y., Zou, S., Ling, Z., Wang, X., Jiang, F., Zeren, Y., Pan, W., Huang, X., and Shen, J.: Ozone pollution around a coastal region of South China Sea: interaction between marine and continental air, *Atmos. Chem. Phys.*, 18, 4277–4295, 10.5194/acp-18-4277-2018, 2018a.

Wang, H., Tan, S., Wang, Y., Jiang, C., Shi, G., Zhang, M., Che, H.: A multisource observation study of the severe prolonged regional haze episode over eastern China in January 2013. *Atmos. Environ.* 89, 807–815, 2014.

Wang, M., Chen, W., Zhang, L., Qin, W., Zhang, Y., Zhang, X., and Xie, X.: Ozone pollution characteristics and sensitivity analysis using an observation-based model in Nanjing, Yangtze River Delta Region of China, *J Environ Sci (China)*, 93, 13-22, 10.1016/j.jes.2020.02.027, 2020.

Wang, Y., Guo, H., Zou, S., Lyu, X., Ling, Z., Cheng, H., and Zeren, Y.: Surface O₃ photochemistry over the South China Sea: Application of a near-explicit chemical mechanism box model, *Environ Pollut*, 234, 155-166, 10.1016/j.envpol.2017.11.001, 2018b.

Whalley, L. K., Stone, D., Bandy, B., Dunmore, R., Hamilton, J. F., Hopkins, J., Lee, J. D., Lewis, A. C., and Heard, D. E.: Atmospheric OH reactivity in central London: observations, model predictions and estimates of in situ ozone production, *Atmos. Chem. Phys.*, 16, 2109-2122, 10.5194/acp-16-2109-2016, 2016.

Wu, X., Li, M., Chen, J., Wang, H., Xu, L., Hong, Y., Zhao, G., Hu, B., Zhang, Y., Dan, Y., and Yu, S.: The

characteristics of air pollution induced by the quasi-stationary front: Formation processes and influencing factors, *Sci Total Environ*, 707, 136194, 10.1016/j.scitotenv.2019.136194, 2020.

Wu, X., Xu, L., Hong, Y., Chen, J., Qiu, Y., Hu, B., Hong, Z., Zhang, Y., Liu, T., Chen, Y., Bian, Y., Zhao, G., Chen, J., and Li, M.: The air pollution governed by subtropical high in a coastal city in Southeast China: Formation processes and influencing mechanisms, *Sci Total Environ*, 692, 1135-1145, 10.1016/j.scitotenv.2019.07.341, 2019.

Xue, L. K., Wang, T., Gao, J., Ding, A. J., Zhou, X. H., Blake, D. R., Wang, X. F., Saunders, S. M., Fan, S. J., Zuo, H. C., Zhang, Q. Z., and Wang, W. X.: Ground-level ozone in four Chinese cities: precursors, regional transport and heterogeneous processes, *Atmos. Chem. Phys.*, 14, 13175-13188, 10.5194/acp-14-13175-2014, 2014.

Xue, L., Gu, R., Wang, T., Wang, X., Saunders, S., Blake, D., Louie, P. K. K., Luk, C. W. Y., Simpson, I., Xu, Z., Wang, Z., Gao, Y., Lee, S., Mellouki, A., and Wang, W.: Oxidative capacity and radical chemistry in the polluted atmosphere of Hong Kong and Pearl River Delta region: analysis of a severe photochemical smog episode, *Atmos. Chem. Phys.*, 16, 9891–9903, 10.5194/acp-16-9891-2016, 2016.

Zeren, Y., Guo, H., Lyu, X., Jiang, F., Wang, Y., Liu, X., Zeng, L., Li, M., and Li, L.: An Ozone “Pool” in South China: Investigations on Atmospheric Dynamics and Photochemical Processes Over the Pearl River Estuary, *J. Geophys. Res.*, 124, 12340-12355, 10.1029/2019jd030833, 2019.

Zhang, K., Duan, Y., Huo, J., Huang, L., Wang, Y., Fu, Q., Wang, Y., and Li, L.: Formation mechanism of HCHO pollution in the suburban Yangtze River Delta region, China: A box model study and policy implementations, *Atmos. Environ.*, 267, 118755, 10.1016/j.atmosenv.2021.118755, 2021a.

Zhang L , Brook J R , Vet R . A revised parameterization for gaseous dry deposition in air-quality models. *Atmos. Chem. Phys.*, 3(2), 2067-2082, 2003.

Zhang, Y., Hong, Z., Chen, J., Xu, L., Hong, Y., Li, M., Hao, H., Chen, Y., Qiu, Y., Wu, X., Li, J.-R., Tong, L., and Xiao, H.: Impact of control measures and typhoon weather on characteristics and formation of PM_{2.5} during the 2016 G20 summit in China, *Atmos. Environ.*, 224, 117312, 10.1016/j.atmosenv.2020.117312, 2020a.

Zhang, Y., Xu, L., Zhuang, M., Zhao, G., Chen, Y., Tong, L., Yang, C., Xiao, H., Chen, J., Wu, X., Hong, Y., Li, M., Bian, Y., and Chen, Y.: Chemical composition and sources of submicron aerosol in a coastal city of China: Results from the 2017 BRICS summit study, *Sci Total Environ*, 741, 140470, 10.1016/j.scitotenv.2020.140470, 2020b.

Zhang, Y. , Xue, L. , Carter, W. , Pei, C. , and Wang, W.: Development of Ozone Reactivity Scales for Volatile Organic Compounds in a Chinese Megacity, *Atmos. Chem. Phys.*, 10.5194/acp-2021-44, 2021

Zhu, J., Wang, S., Wang, H., Jing, S., Lou, S., Saiz-Lopez, A., and Zhou, B.: Observationally constrained modeling of atmospheric oxidation capacity and photochemical reactivity in Shanghai, China, *Atmos. Chem. Phys.*, 20, 1217-1232, 10.5194/acp-20-1217-2020, 2020.

781